Study of Relativistic Electron Beam Propagation in the Atmosphere-Ionosphere-Magnetosphere
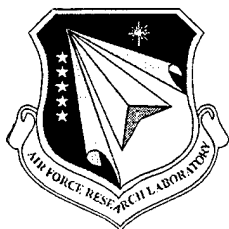
Brian E. Gilchrist
George Khazanov
Linda Krause
Torsten Neubert

University of Michigan
3003 S. State Street
Ann Arbor, MI 48109-1274

12 Dec 2001

AIR FORCE RESEARCH LABORATORY
Space Vehicles Directorate
29 Randolph Rd
AIR FORCE MATERIEL COMMAND
HANSCOM AFB, MA 01731-3010

20020702 045

"This technical report has been reviewed and is approved for publication"

SHU T. LAI
Program Manager

MARK WILSON, Capt, USAF
Team Leader

This report has been reviewed by the ESC Public Affairs (PA) and is releasable to the National Technical Information Service (NTIS)

Qualified requesters may obtain additional copies from the Defense Technical Information Center (DTIC). All others should apply to the National Technical Information Service (NTIS)

If your address has changed, if you wish to be removed from the mailing list, or if the addressee is no longer employed by your organization, please notify AFRL/VSOS-IM, 29 Randolph Road, Hanscom AFB, MA 01731-3010. This will assist us in maintaining a current mailing list.

Do not return copies of this report unless contractual obligations or notices on a specific document require that it be returned.

REPORT DOCUMENTATION PAGE

The public reporting burden for this collection of information is estimated to average 1 hour per response, including the time for reviewing instructions, searching existing data sources, gathering and maintaining the data needed, and completing and reviewing the collection of information. Send comments regarding this burden estimate or any other aspect of this collection of information, including suggestions for reducing the burden, to Department of Defense, Washington Headquarters Services, Directorate for Information Operations and Reports (0704-0188), 1215 Jefferson Davis Highway, Suite 1204, Arlington, VA 22202-4302. Respondents should be aware that notwithstanding any other provision of law, no person shall be subject to any penalty for failing to comply with a collection of information if it does not display a currently valid OMB control number.
PLEASE DO NOT RETURN YOUR FORM TO THE ABOVE ADDRESS.

1. REPORT DATE *(DD-MM-YYYY)*	2. REPORT TYPE	3. DATES COVERED *(From - To)*
12-12-2000	Scientific, Final	June 1996-Mar 31, 2000

4. TITLE AND SUBTITLE
Study of Relativistic Electron Beam Propagation in the Atmosphere-Ionosphere-Magnetosphere

5a. CONTRACT NUMBER
F19628-96-K-0004

5b. GRANT NUMBER

5c. PROGRAM ELEMENT NUMBER
61102F

6. AUTHOR(S)
Brian E. Gilchrist
George Khazanov
Linda Krause
Torsten Neubert

5d. PROJECT NUMBER
2311

5e. TASK NUMBER
GA

5f. WORK UNIT NUMBER
MC

7. PERFORMING ORGANIZATION NAME(S) AND ADDRESS(ES)
University of Michigan
3003 S. State Street
Ann Arbor, MI 48109-1274

8. PERFORMING ORGANIZATION REPORT NUMBER

9. SPONSORING/MONITORING AGENCY NAME(S) AND ADDRESS(ES)
Air Force Research Laboratory/VSBXT
29 Randolph Road
Hanscom AFB, MA 01731-3010

10. SPONSOR/MONITOR'S ACRONYM(S)

11. SPONSOR/MONITOR'S REPORT NUMBER(S)
AFRL-VS-TR-2001-1505

12. DISTRIBUTION/AVAILABILITY STATEMENT
Approved for public release; distribution unlimited

13. SUPPLEMENTARY NOTES

14. ABSTRACT
Models for propagation physics and associated ionospheric/atmospheric modification have been developed for the space-based injection of relativistic (E ~ 1-100 MeV) electron beams. Initial evaluations of beam propagation effects in the ionosphere, magnetosphere, and atmosphere have been conducted. The overall goal of this work was to develop computational tools and use them to better assess relavistic beam launch, propagation, and interaction with the space environment and atmosphere. Computational tools developed and then applied to this problem. include models addressing: beam propagation using an envelope equation; integrated beam-atmosphere interactions (This model contains time-dependent chemistry effects necessary to compute optical emissions as a function of altitude); beam launch and propagation using particle-in-cell (PIC) techniques; and magnetospheric propagation and plasma transport (Khazanov models). It is concluded that for practical beam energies and currents the beam propagation is stable. This is done theoretically and using the PIC modeling. Over long distance propagation the Khazanov models were able to show hat the beam particles will scatter in pitch-angle and relative location, but lifetimes are expected to be similar to those found for the radiation belts for nearly equatorial mirroring injection.

15. SUBJECT TERMS
Relativistic electron beam
Ionosphere
Atmosphere
Magnetosphere
Particle-in-cell

16. SECURITY CLASSIFICATION OF:			17. LIMITATION OF ABSTRACT	18. NUMBER OF PAGES	19a. NAME OF RESPONSIBLE PERSON
a. REPORT	b. ABSTRACT	c. THIS PAGE			Shu T. Lai
Uncl	Uncl	Uncl	Unl		19b. TELEPHONE NUMBER *(Include area code)* 781 377-2932

Contents

1. Introduction

1.1 Background

In the late 1980's it was determined that small relativistic electron beam linear accelerators (linac's) had been reduced in size to the point where they could be feasibly flown onboard spacecraft and sub-orbital rockets [*Banks et al.*, 1987; *Banks et al.*, 1990]. Ionospheric modification by beams of this energy can create significant ionization and steep potential gradients resulting from the interaction of the relativistic (MeV) beams with the surrounding environment. These beams should be capable of achieving deep penetration into the lower ionosphere and even into the upper stratosphere when fired directly downwards along the Earth's magnetic field from an orbital or sub-orbital spacecraft.

Earlier, the Air Force sponsored preliminary research with the University of Michigan to assess the practical aspects of relativistic beam propagation including the extent a relativistic electron beam was scattered laterally by collisions with the neutral atmosphere as it propagates downwards into the atmosphere from a space-based platform. It was found that the beam is highly collimated by the magnetic field, and therefore well suited for ionospheric modification-type experiments. This study discussed a number of scientific investigations that could be done with relativistic electron beams. They include: (1) Study of the energetic electron population in the magnetosphere, (2) Modification of the atmospheric electric potential structure, and (3) Modification of chemical reaction paths in the middle atmosphere stimulated by naturally precipitating relativistic electrons. In a later study *Neubert et al.* [1996], also showed that beam confinement by the external axial magnetic field significantly reduces the amount of radial expansion due to small-angle scattering and inelastic collision losses, constraining the beam's radius to be less than its gyroradius at a 90° pitch angle. These initial results provided sufficient encouragement to scientists at the Air Force Research Laboratory (AFRL) to consider that long-range propagation of MeV electrons beams in the Earth's upper atmosphere is theoretically feasible.

The Spaceborne Linear Accelerator System (SLINAC) is a program designed to demonstrate the viability of injecting relativistic ($E \sim$ MeV) electron beams into the earth's upper atmosphere/ionosphere. Motivating forces behind this mission include [*Jost*, 1993]:

- Upper atmosphere/ionosphere/magnetosphere research
- Orbital debris detection and mitigation
- Atmospheric ozone depletion monitoring and mitigation
- RF scattering screens
- Department of Energy directed beam considerations

The beam generator developed for the Air Force in this program has the following characteristics that are used here for practical considerations:

- beam energy: 5 MeV
- beam current: 100 mA
- pulse length: 4 μs
- duty cycle: 0.001

1.2 Goals

The overall goal of the work of this grant was to develop computational tools and use them to better assess relativistic electron beam launch and propagation from space platforms and its interaction with the space environment and atmosphere. To accomplish this goal, several computational tools were developed and then applied to this problem. These include:

1. **The paraxial envelope model of beam propagation:** A set of one-dimensional equations to calculate the beam radius and energy was applied to propagation in the atmosphere, ionosphere, and magnetosphere. The model was also used to support an analysis of various instability growth rates.

2. **Relativistic Beam-Atmosphere Interaction (RelBAI) model:** A model based on the two-stream approach, with extension to relativistic energies using the paraxial envelope equations

2

was developed to model energy degradation and optical emissions resulting from electron - neutral atmosphere collisions.

3. **Particle-in-Cell (PIC) beam launch and propagation model:** The TRISTAN electromagnetic and relativistic PIC code [*Buneman et al.*, 1993] was applied to beam injection from a spacecraft to asses spacecraft charging, beam degradation, and questions of stability.

4. **Khazanov plasma transport model:** Based on the Boltzman kinetic equation for the electron distribution, the Khazanov 4D and 5D plasma transport models were extended to relativistic energies. The time dependent behavior of relativistic beam flux and its secondaries in the atmosphere-ionosphere-magnetosphere was modeled.

The first two are discussed in the following section with the latter two covered in the next two sections.

2. The Paraxial Envelope Equations and RelBAI Model

In order to guarantee a successful mission in which the heritage of an accelerator such as the LINAC system may be established, it is useful to quantify the beam propagation characteristics that are expected during an active experiment in the terrestrial space environment. Specifically, the areas of interest covered by this study include:

- Analytical Description of Beam Propagation. As an extension to the study by *Neubert et al.* [1996], the beam envelope equations have been used to predict beam propagation characteristics of interest (energy, radius, divergence) as a function of altitude over a variety of injection parameters, including beam energy $(1 - 100 \, \text{MeV})$, divergence $(0.01 - 0.1 \, \text{radians})$, and relativistic electron beam study current $(0.1 - 10^4 \, \text{A})$. Effects of beam-generated electric and magnetic fields were included in the analysis.

- Beam-Plasma Interactions (BPI). When high current beams $(I > 100 \, \text{A})$ are considered, it is appropriate to examine the interaction of the beam with the surrounding space plasma. A first-

order analysis of the BPI was performed for relativistic electron beams (REBs) propagating in a model terrestrial ionospheric environment.

- Diagnostics for Active Space Experiments with REBs. The Relativistic Beam-Atmosphere Interactions (RelBAI) model has been constructed in order to provide scientific and technological investigators with a tool to quantify physical signatures, such as optical emissions and ionization, resulting from the REB precipitation in a model atmosphere. This model provides a means of predicting the intensity of these products that would aid in the selection of the appropriate instrumentation for detection and characterization of a propagating REB during an actual test in space.

This section presents a summary of the findings from the analysis of REB dynamics, stability, and the resulting ionospheric modification during propagation in a model terrestrial upper atmospheric and ionospheric environment. References to published technical reports are noted in each section to direct the interested reader to documents detailing this research.

2.1 Beam Dynamics

We have adopted a set of analytical equations that describe relativistic electron beam propagation in the paraxial approximation (small pitch angle and narrow divergence) to a set of beams that are propagating in the Earth's near space environment. The model has application to naturally occurring space science phenomena, but our analysis is targeted on the ideal case of artificially injecting relativistic electrons beams of various energies (1 - 100 MeV), divergence values (0.01 - 0.1 radians), and currents (0.1 - 10^4 A). These beams are simulated as injected downwards along a constant vertical magnetic field (0.4 G), and they propagate through a model atmosphere and ionosphere representative of a night-time environment with moderate solar activity (sunspot number ~ 30). The model atmosphere and ionosphere used for these computations is detailed in *Habash Krause* [1997a]. The radial expansion of the beam as the electrons collide with the atmospheric neutrals is described by the paraxial ray equation; energy loss due to elastic and inelastic collisions and electron-neutral bremsstrahlung is used to determine pitch angle

4

scattering (emittance growth) of the beam. The complete set of envelope equations are given as [*Lawson*, 1988; *Humphries*, 1990; *Neubert et al.*, 1996]:

$$r'' = -\frac{\gamma' r'}{\beta^2 \gamma} - \left(\frac{qB_z}{2\beta\gamma m_e c}\right)^2 r + \frac{\langle\theta^2\rangle}{r} + \frac{K}{r} \qquad (2.1)$$

$$\frac{d\langle\theta^2\rangle}{dz} = \frac{d\langle\theta^2\rangle}{dz}\bigg|_c + \frac{2\gamma}{\gamma^2-1}\langle\theta^2\rangle\frac{d\gamma}{dz} \qquad (2.2)$$

$$\frac{d\langle\theta^2\rangle}{dz}\bigg|_c = \frac{16NZ(Z+1)r_e^2}{\gamma^2\beta^4}\ln\left[\frac{204}{Z^{0.333}}\right] \qquad (2.3)$$

$$\frac{d\gamma}{dz}\bigg|_c = -\frac{2\pi NZr_e^2}{\beta^2}\left[\ln\left(\frac{1}{2}\left(\frac{m_e c^2}{W_o}\right)^2\beta^2\gamma^2(\gamma-1)\right) - \ln^2\left(\frac{2}{\gamma}-1+\beta^2\right) + \frac{1}{\gamma^2} + \frac{(1-1/\gamma)^2}{8}\right] \qquad (2.4)$$

$$\frac{d\gamma}{dz}\bigg|_r \cong \frac{-4NZ(Z+1)(\gamma-1)r_e^2}{137}\left(\ln(2\gamma-2)-1\right) \qquad (2.5)$$

$$K = \frac{2I_b}{\beta^2 I_A}\left(\frac{1}{\gamma^2}-f_e\right) \qquad (2.6)$$

where Equations 2.1 through 2.6 respectively describe the radial expansion of the beam, the emittance growth due to all processes, the emittance growth specifically due to elastic collisional processes, the energy lost by the beam due to electron-neutral collisions, the bremsstrahlung energy radiated away from the beam, and the beam perveance.

Sample computations were performed for five beam energies ranging from 1.0 MeV to 100 MeV. All beams carried a current of 0.1 A and were injected with an initial divergence of 0.01 radians. Figures 2.1 through 2.3 respectively show the radius, mean-squared divergence, and fractional energy loss, which are computed at each altitude from injection (140 km) down to the altitude at which the bulk of the energy is lost. These results show that all beams maintain a slowly-varying radius until they encounter a region in the atmosphere that is dense enough to cause significant emittance growth via electron-neutral collisions. The altitude at which this occurs depends on the initial energy of the beam, which is consistent with the fact that the interaction cross section decreases with increasing primary beam energy.

The atmospheric range increases monotonically with beam primary energy ($R(E) = 3.247E^{1.043}$, R in kg/m^2, E in MeV), but it is found to be independent of divergence and current. The range values agree well with those computed in the continuous loss approximation [*Berger and Seltzer*, 1964], but they diverge slightly as lower energies ($E \leq 5$ MeV) are approached (Figure 2.4). See *Habash Krause* [1997a] for further details on model construction and computations. Beam propagation following upward injection has been investigated with this model and is described in *Habash Krause et al.* [2000].
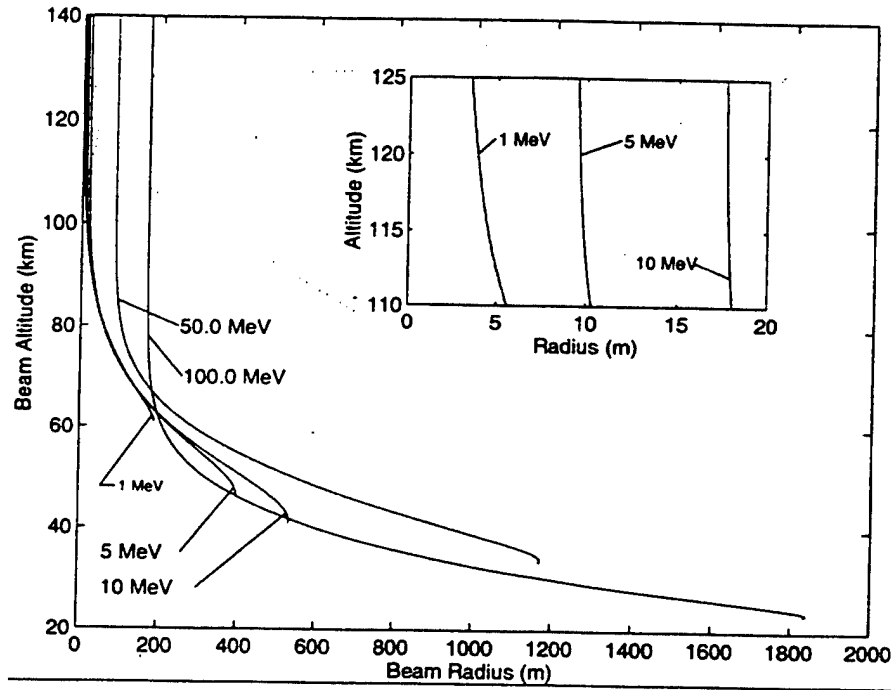

Figure 2.1: Beam radius as a function of altitude for downward propagation. Injection current and divergence values are 0.1 A and 0.01 radians, respectively. Five beams are examined with injection energies E - [1, 5, 10, 50, 100] MeV. Inset figure contains an enlarged view of the expansion of the 1, 5, and 10 MeV beams as they enter the collisional regime.
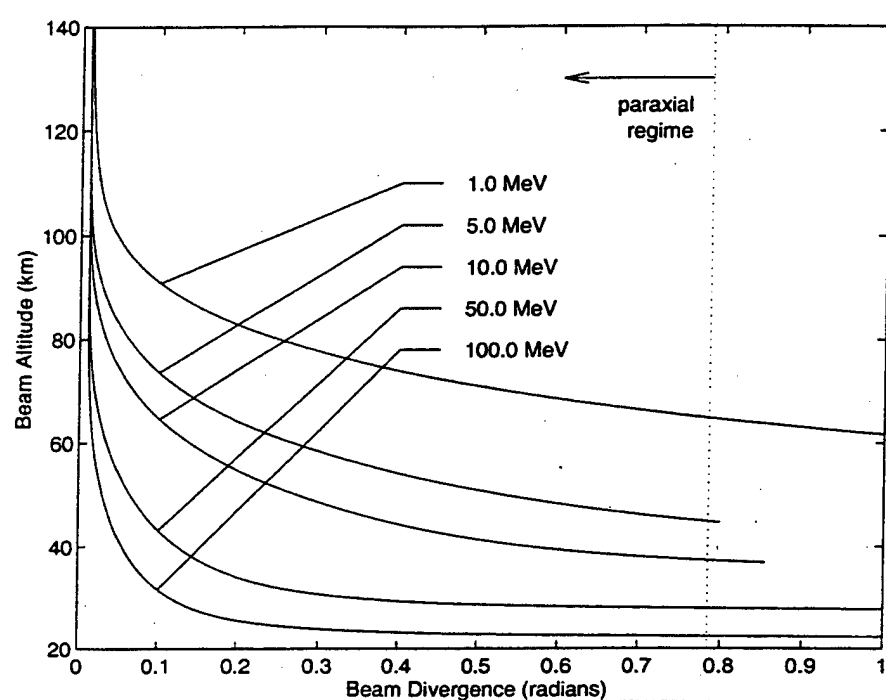
Figure 2.2:   Beam divergence as a function of altitude for downward propagation.   Injection current and divergence values are 0.1 A and 0.01 radians, respectively. Five beams are examined with injection energies E - [1, 5, 10, 50, 100] MeV. Paraxial limit (0.78 radians) is shown for reference.
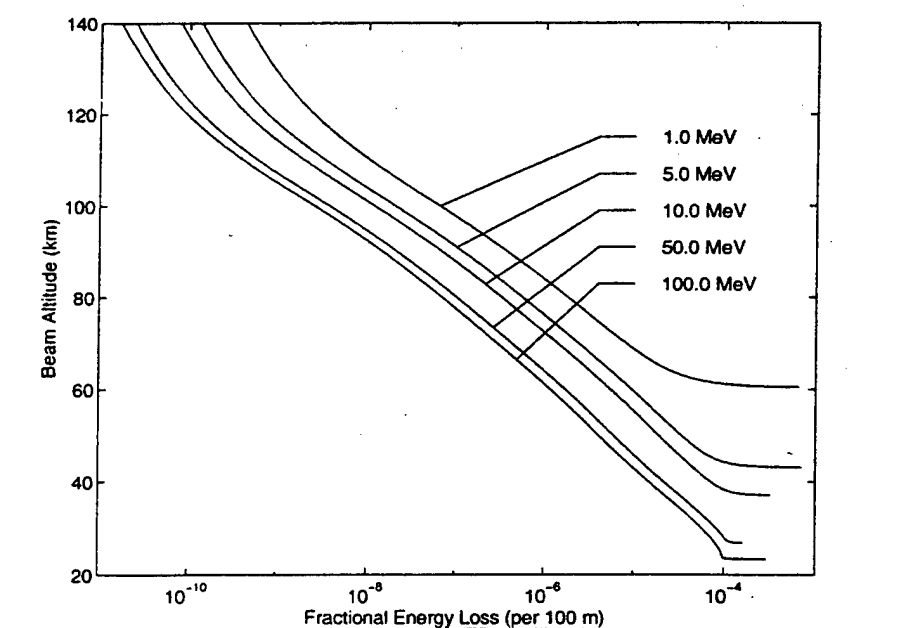

Figure 2.3:   Beam fractional energy loss per electron as a function of altitude for downward propagation.   Injection current and divergence values are 0.1 A and 0.01 radians, respectively. Five beams are examined with injection energies E - [1, 5, 10, 50, 100] MeV.
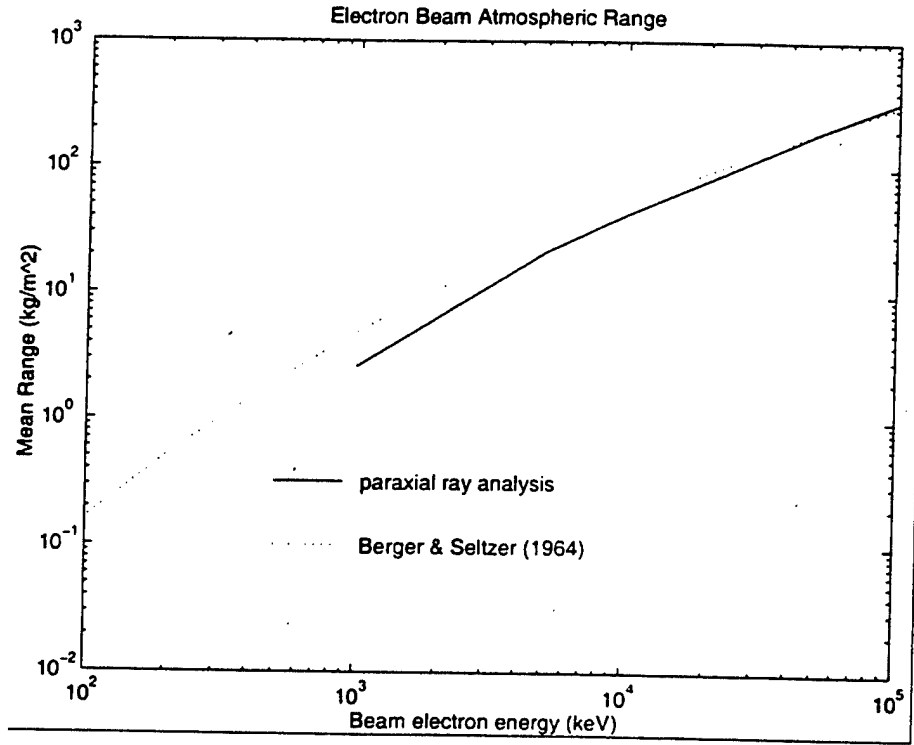
Figure 2.4: Electron beam atmospheric collisional range: Comparison with previously published results.

2.2 Beam Stability

Growth rates for several instabilities, including the two-stream, resistive hose, and ion hose, were assessed. The equations governing the time rate of growth of the instabilities are:

$$\tau_{TS} = \frac{2}{\sqrt{3}} \left(\frac{2}{\omega_{pb}^2 \omega_{pe}} \right)^{\frac{1}{3}}$$

(2.7)

$$\tau_{IH} = \frac{2\pi}{\omega_{\beta i}} f_e^{1/2}$$

(2.8)

$$\left(1/\tau_{RH} \right)^2 = -\frac{1}{2} \left(\frac{\omega_{\beta e}^2 \omega^2 \tau_d^2}{1+\omega^2 \tau_d^2} + \left(\frac{\omega_{cb}}{2} \right)^2 \right) + \frac{1}{2} \sqrt{ \frac{\omega_{\beta e}^2 \omega^2 \tau_d^2}{1+\omega^2 \tau_d^2} \left(\omega_{\beta e}^2 + \frac{\omega_{cb}^2}{2} \right) + \left(\frac{\omega_{cb}}{2} \right)^4 }$$

(2.9)

where equations 2.7 through 2.9 respectively describe the characteristic growth periods of the two-stream, ion hose, and resistive hose instabilities. We seek these values because if the growth period of an instability is comparable to or shorter than the length of a beam pulse, the pulse may be affected by the instability.

8

Additionally, beam susceptibility to Weibel filamentation was examined using the filamentation stability factor, given as:

$$\xi = \frac{\dfrac{\omega_{pe}^2 T_b}{m_e c^2 \gamma^2} + \omega_{cb}^2}{\omega_{pb}^2 \beta^2 \gamma + \dfrac{\omega_{pe}^2 T_p}{m_e c^2 \gamma^2}} \qquad (2.10)$$

where $\xi > 1$ signifies that the beam is stable against filamentation.

Using the same model atmosphere/ionosphere as those employed in the computation of beam dynamics, instability growth periods and filamentation stability factors were computed for downward-injected beams of several initial energies (1 – 10 MeV), divergence values (0.01 - 0.1 radians), and currents (1 - 10^4 A), and at noon and midnight conditions. An injection altitude of 350 km was selected to investigate the worst-case scenario of propagation through the F region. It was found that within this range of parameters, all of these beams, when pulsed at μs intervals, are stable against filamentation and ion hose, but low energy, high current beams may be subject to the resistive hose and two-stream instabilities. Sample computations appear in Figures 2.5 through 2.10, with initial beam parameters given in the captions. The ramifications of the onset of any of these instabilities include enhanced emittance growth, heating and ionization of the ambient plasma environment, and, in some of the more esoteric events, current multiplication. These factors may play a significant role in the description of the beam dynamics. If so, a unified approach to solving the dynamics equations with these effects included would be necessary for a complete and accurate description of relativistic electron beams propagating in the Earth's atmosphere. A detailed treatment of the instability analysis appears in *Habash Krause* [1997b].
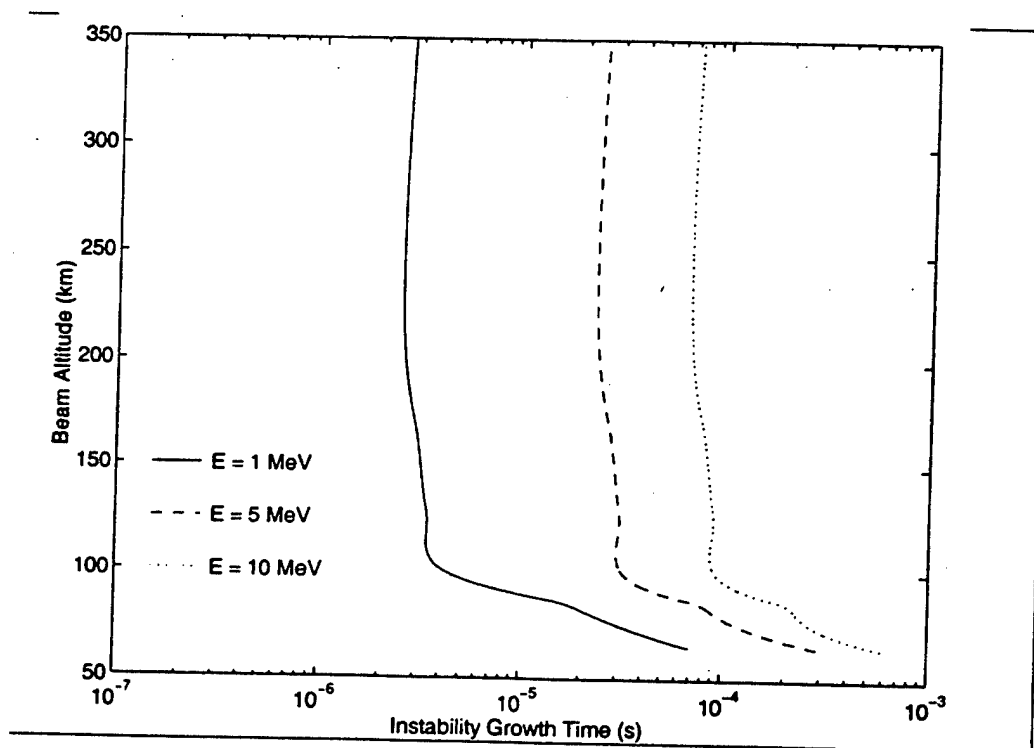
Figure 2.5:   Two-stream instability growth period for daytime propagation; I = 0.1 A and $<\theta^2>_o$ = 0.05 rad.
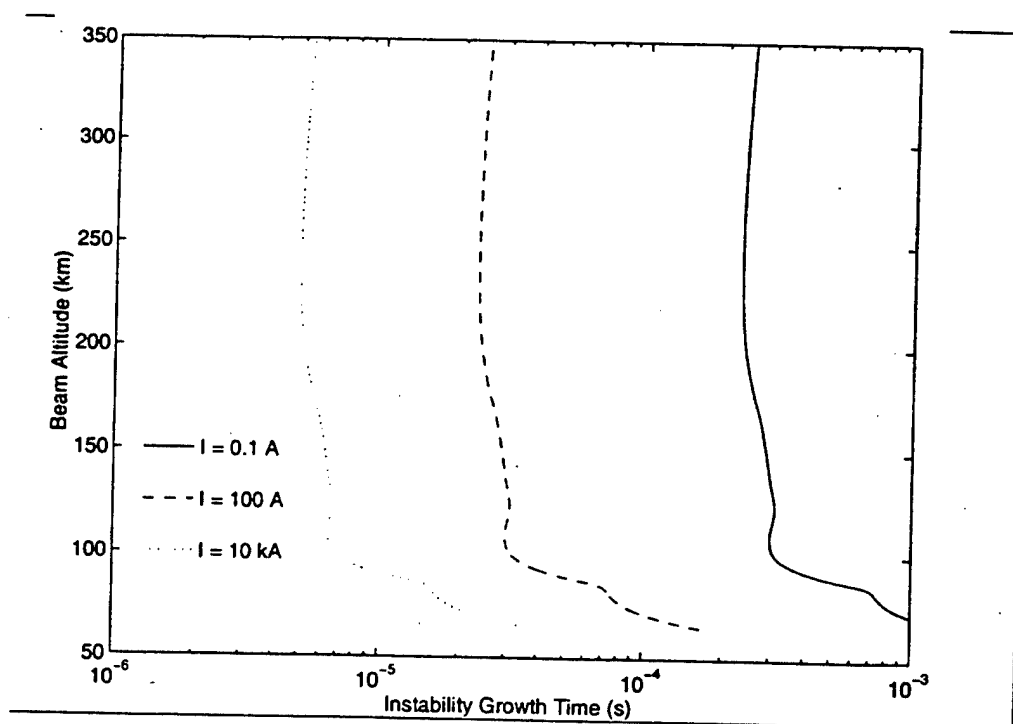
Figure 2.6:   Two-stream instability growth period for daytime propagation; E = 5 MeV and I = 0.1 A.
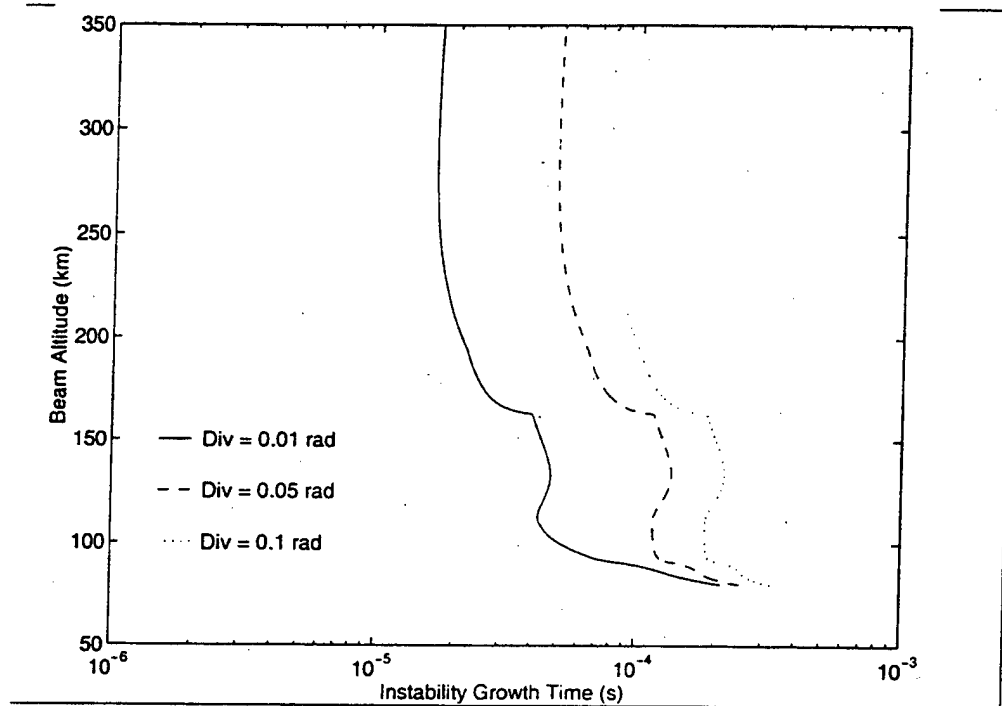
Figure 2.7: Two-stream instability growth period for nighttime propagation; $E = 10$ MeV and $<\theta^2>_0 = 0.1$ rad.

Figure 2.8: Ion hose instability growth period for nighttime and daytime propagation of all space-charged neutralized beams.

Figure 2.9: Resistive hose instability growth period for propagation, independent of time of day; I = 0.1 A and $<\theta^2>_o = 0.05$ rad.

Figure 2.10: Weibel filamentation stability growth parameter for daytime propagation; I = 0.1 A and $<\theta^2>_o = 0.05$ rad.

2.3 The RelBAI Model
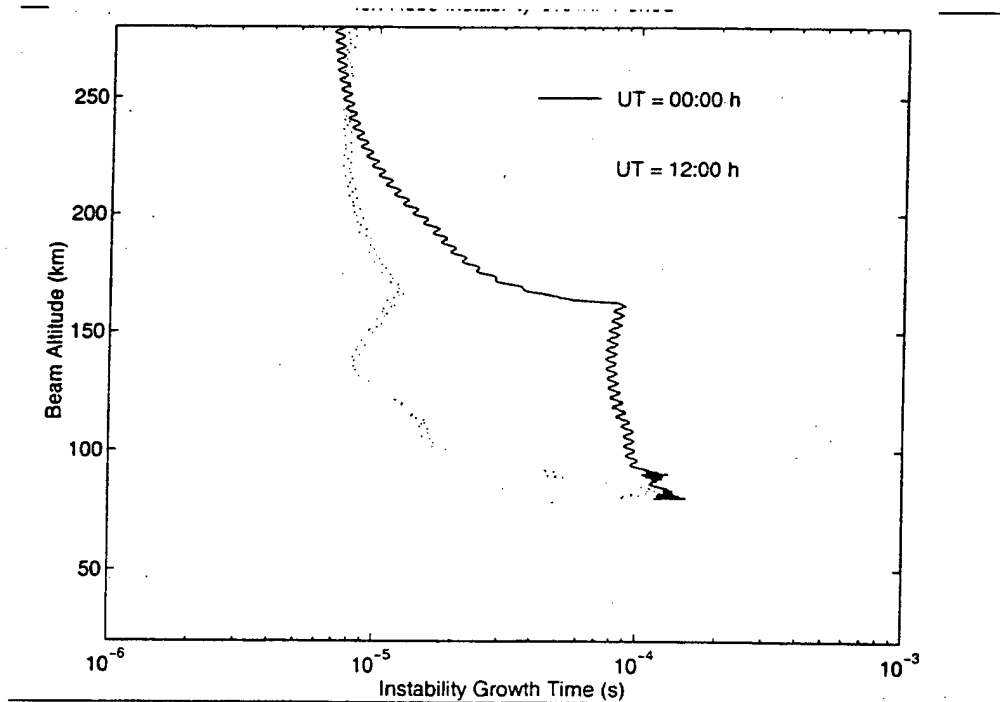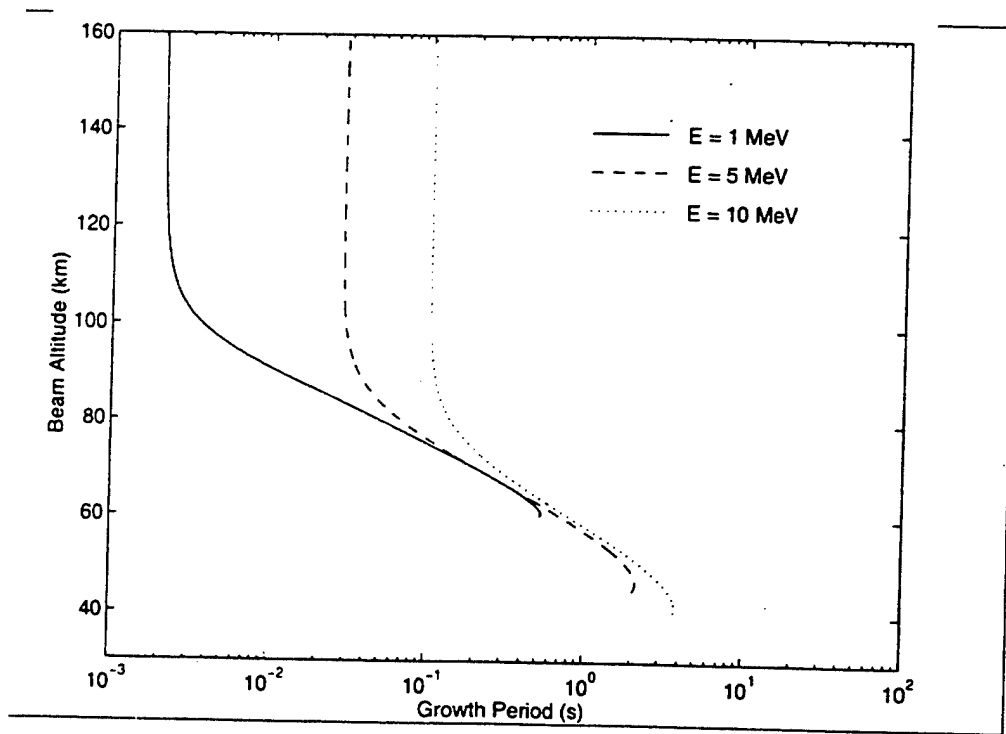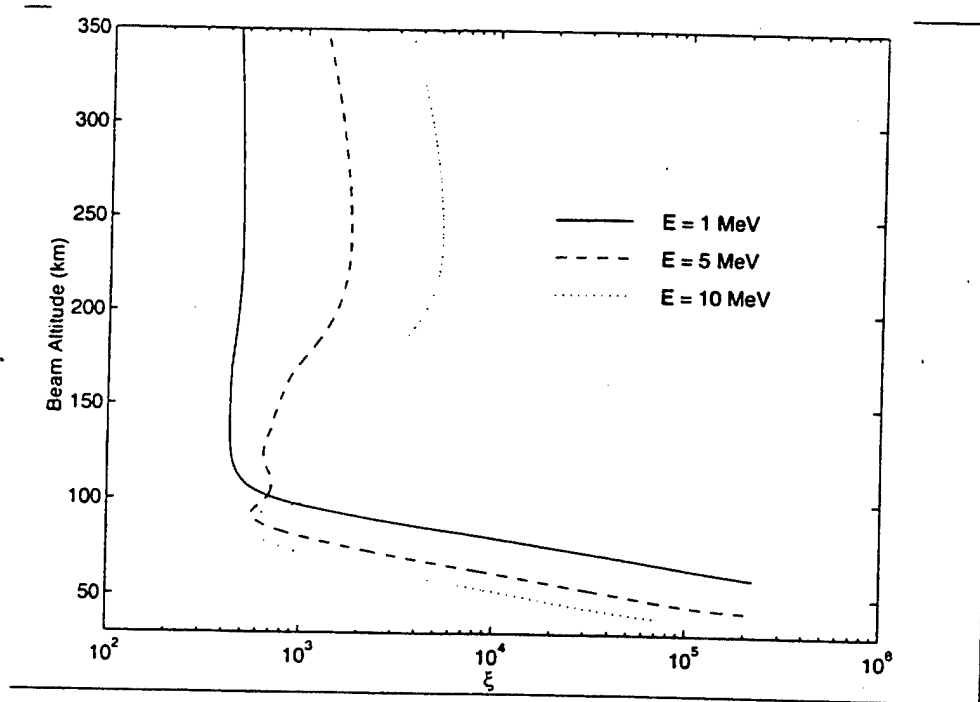
The RelBAI model was constructed for the purpose of providing a tool by which investigators interested in detailed specifications of products of the relativistic BAI can compute quantities of interest with minimal computer resources. The model is comprised of several established analytical algorithms, each of which is designed with its own set of input and output parameters. The idea is to have a "black box" model that allows users to enter beam parameters, environmental models, and cross section data; quantities of interest are output in steady state. The model is modular in nature, and input/output parameters of the modules are wired together which form the connections of the modules (Figure 2.11). This arrangement facilitates specialization of the code: investigators may build upon the model by connecting new modules at the appropriate places. As a demonstration of the capabilities of this model, several quantities of interest for remote sensing purposes were computed, including total ionization, bremsstrahlung production and production of several excited states of neutral and ionized molecular nitrogen resulting from the propagation of a 5 MeV beam through the atmosphere. For example, ionization of major neutral constituents appears in Figure 2.12. We note that the model requires validation with experimental data once the SLINAC is operational, but under this contract, we were at least able to demonstrate consistency with certain acceptable values associated with electron precipitation in the terrestrial atmosphere. For example, it is well-known that the average amount of energy deposited per ionization event in the atmosphere is ~35 eV, and our results are comparable to this number (Figure 2.13). See *Habash Krause* [1998a] for a detailed treatment on the construction and use of the RelBAI model.

In the next section, the bremsstrahlung fluxes computed from this model are used to predict photon energy-dependent spectra incident on detectors on balloons or satellites in low Earth orbit.
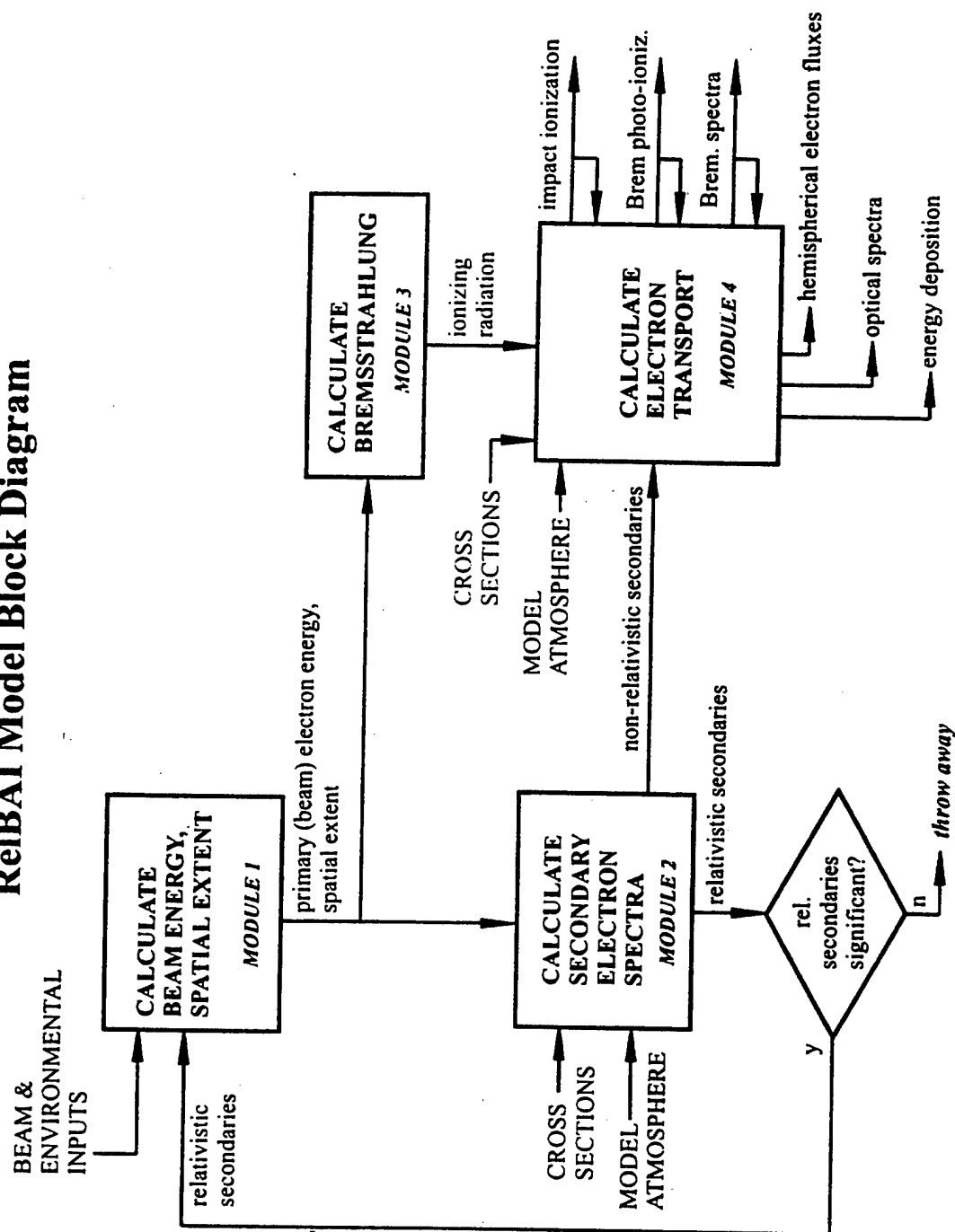
Figure 2.11: Block diagram of the RelBAI model.

14

Ionization by fast electrons, E = 5 MeV, I = 1.0 A
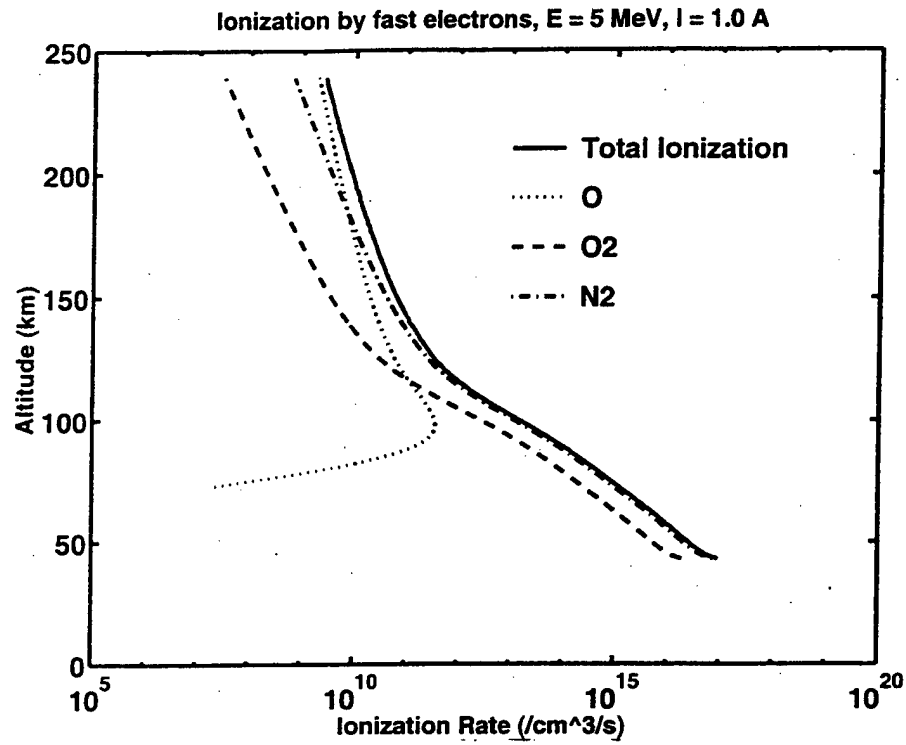

Figure 2.12: Ionization of major atmospheric neutral constituents from cascading electrons for initial beam energy of 5 MeV.

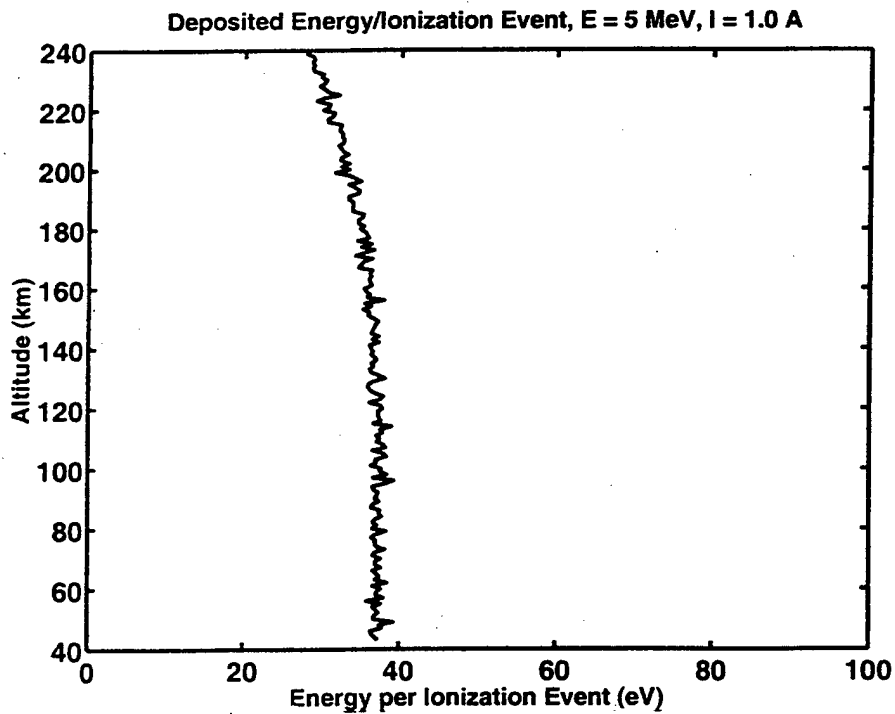**Deposited Energy/Ionization Event, E = 5 MeV, I = 1.0 A**

Figure 2.13: Energy deposition per ionization event from cascading electrons for initial beam energy of 5 MeV.

2.4 Remote Sensing of Beam-Induced Bremsstrahlung

Bremsstrahlung flux spectra, differential in photon energy and which are incident on detectors at balloon and Low-Earth Orbit (LEO) satellite altitudes, are computed. Attenuation of radiation by the atmosphere is included, and a mass attenuation coefficient, dependent on photon energy, incorporates intensity loss mechanisms of interest for the photon energy regime under consideration. These scattering mechanisms include photoelectric effect, Rayleigh scattering, Compton scattering, electron-positron pair production, and photonuclear interaction. The geometry for computations of the bremsstrahlung flux measured by imagers aboard satellites in LEO is shown in Figure 2.14. The attenuated bremsstrahlung measured by satellite at large horizontal distances from the beam column is larger by several orders of magnitude than that measured by the satellite detector at small horizontal displacements (Figure 2.15). A balloon detector may intercept more bremsstrahlung, by several orders of magnitude, as in the situation examined here, than the downward-looking satellite detector if the balloon detector is oriented with its look direction coincident with the beam source line of sight (compare Figures 2.15 and 2.16). However, it may be impractical to have sufficient knowledge of the location of the bremsstrahlung source before the balloon detector can be reoriented to look directly at the beam. Perhaps a balloon payload with x-ray sensors looking in each of the four cardinal directions would be necessary. See *Habash Krause* [1998b] for details on these computations.
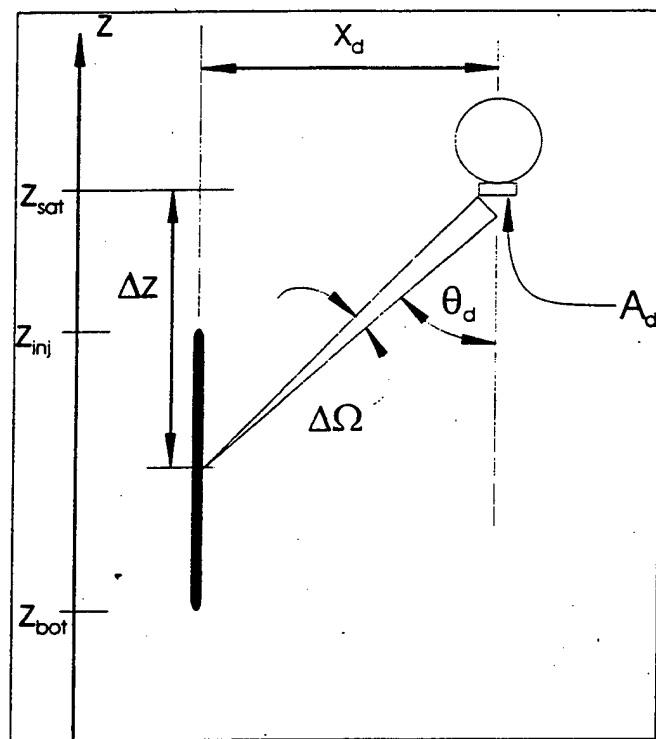
Figure 2.14: Schematic of geometry for bremsstrahlung flux detection at LEO altitudes.
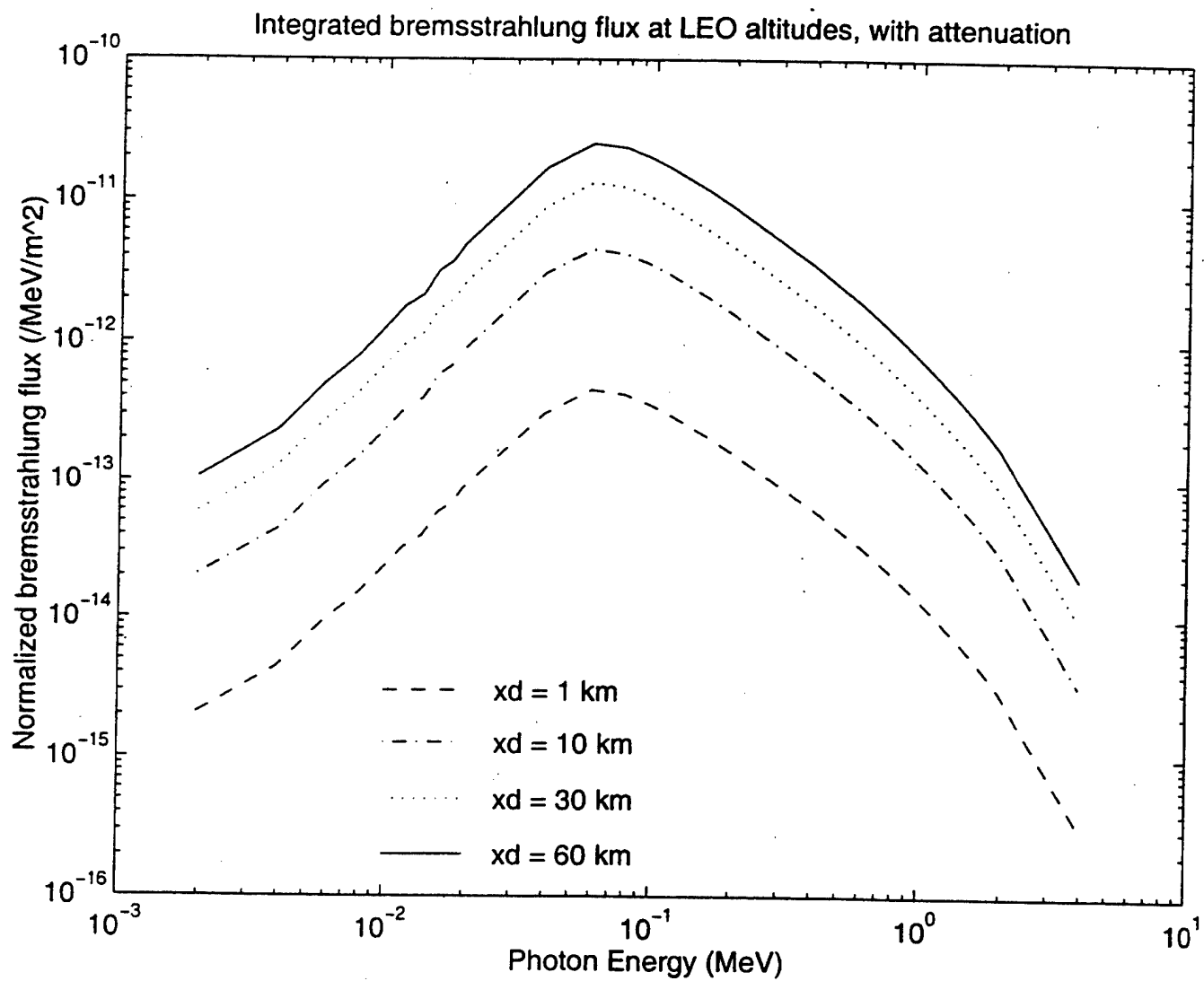
Figure 2.15: Integrated bremsstrahlung flux incident on a satellite detector at LEO altitudes. Atmospheric attenuation is included.

Integrated bremsstrahlung flux at balloon altitudes, with attenuation
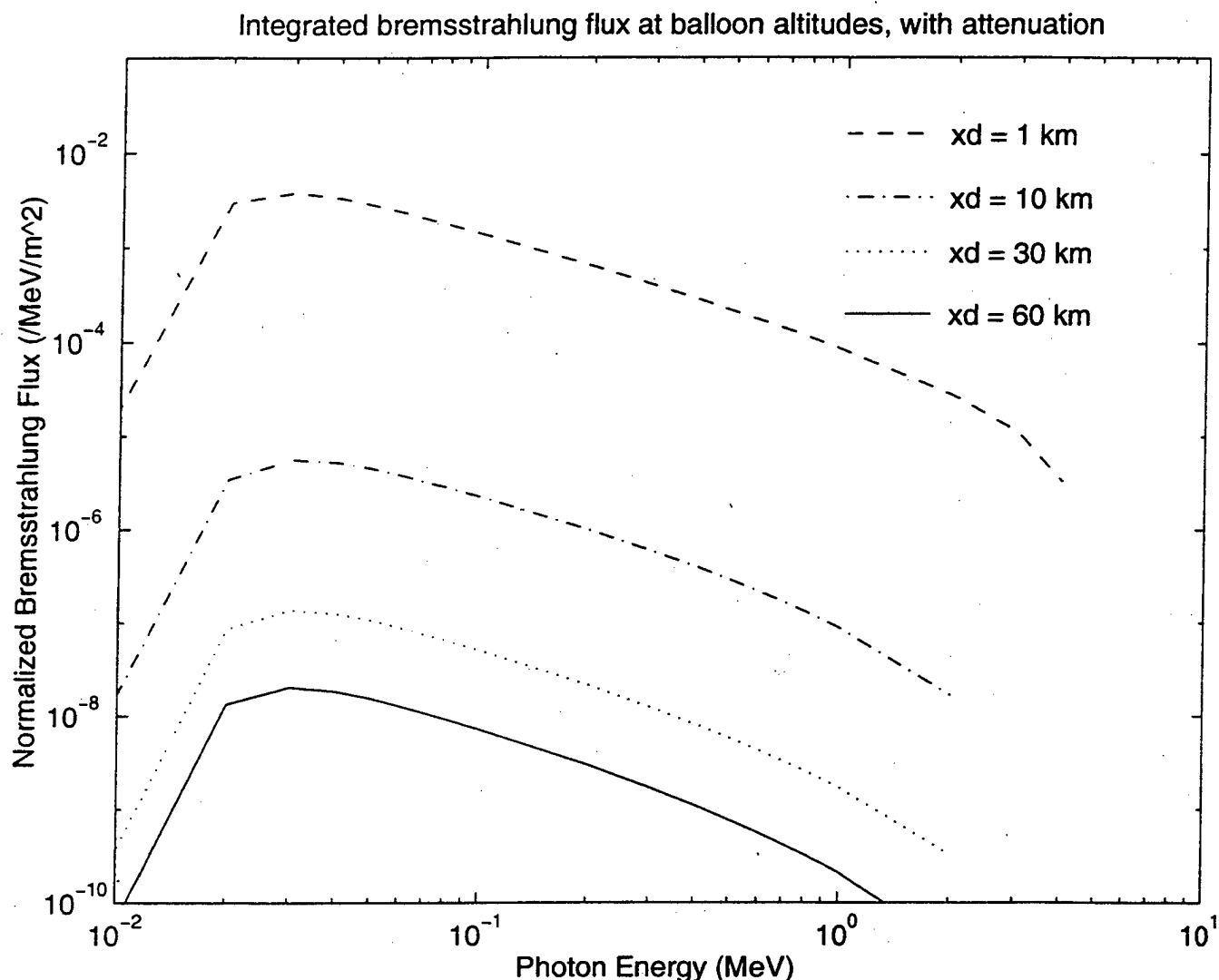
Figure 2.16: Integrated bremsstrahlung flux incident on a detector at balloon altitudes. Atmospheric attenuation is included

2.5 RelBAI Summary and Continuing Work

The research completed under the contract has laid the foundation for continuation of theoretical studies necessary to plan for the heritage launch of the SLINAC 5 MeV electron beam. The next major step in the development of this research was accomplished on-site at AFRL/VSBS with the completion of a relativistic electron auroral model. This model contains the time-dependent chemistry necessary to compute optical emissions as a function of altitude. It was shown that, for 5 MeV electron beams injected directly downward into the Earth's atmosphere along a constant, vertical magnetic field, the 427.8 nm, 391.4 nm, and 337.1 nm molecular nitrogen lines are strong in intensity, with production

rates several orders of magnitude greater in than those of the O lines examined (557.7 nm and 630.0-636.4 nm doublet). It was shown that the production of 337.1 nm is insensitive to compositional change and has a quenching height lower in altitude than the propagation depth of a 5 MeV electron beam, and thus the signature may be suitable as an indicator of electron flux for beams of comparable energy. The ratio of 427.8 nm to 391.4 nm emissions was found to be relatively insensitive to compositional changes, and the ratio varies with altitude at lower altitudes, suggesting that it may suitable for inference of characteristic beam energy for MeV electron beams (see *Habash Krause et al.* [1999] for details on the relativistic electron auroral model).

3. 3-D Relativistic Particle-in-Cell (PIC) Simulations of The Relativistic Beam Injection Process

3.1 Background

PIC simulations of relativistic electron beam dynamics have been undertaken to investigate the beam injection process from a spacecraft in order to give realistic initial conditions of beam parameters for large-scale models of beam propagation in the Earth's atmosphere-ionosphere-magnetosphere [*Neubert et al.*, 1996; *Kazanov et al.*, 1999]. In particular, the following questions have been addressed:

- The proper handling of spacecraft charging effects on the beam in a 3D code. This is an important issue because beams will often not escape a spacecraft environment with the full energy because of electric charging of the spacecraft.

- Kinetic effects influence beam propagation in the plasma. PIC simulations are done to help complement the analytical beam dynamics analysis. in particular to address the question of beam neutralization and beam stability.

The beam pulses under investigation are those of the linac being tested for flight by the Air Force [*Jost*, 1993]. The parameters are shown in Table 3.1.

Table 3.1: *Relativistic beam pulse parameters*

Ib	Eb	τb	Td	ao	ε	nb°	ωpb°
0.1 A	5 MeV	4 μs	0.001	1.5 mm	0.018 cm-rad	$2.9 \times 10^{14} m^{-3}$	2.9×10^{8} rad/s

I_b is the beam current, E_b the beam energy, τ_b the beam pulse length, T_d the duty cycle, a_o the beam diameter at injection, ε the beam emittance, $n_b{}^o$ the density at injection, and $\omega_{pb}{}^o$ the beam plasma frequency at injection: $\omega_{pb}{}^{o2} = q^2 n_b{}^o / \varepsilon \gamma m_e$, where γ is the relativistic factor.

Simulations were first performed in 2D, but it was soon realized, that 3D should be attempted within the framework of the limited effort available in this research. The 3D simulations are performed using the TRISTAN electromagnetic and relativistic particle code [*Buneman et al.*, 1993]. The code uses local updates of the fields from particle motions, rather than Poisson's equation. While this scheme makes the code fast, it is required, that the experimental conditions are described self-consistently within the simulation domain. It is important, therefore, to incorporate the beam source and the spacecraft in the simulation domain with care.

Code developments during this study include:

- Self-consistent spacecraft charging due to beam pulse emission has been included, and the appropriate scaling laws between simulations and the real world for spacecraft charging studies have been identified.

- The option of changing to a moving frame which follows the beam pulse has been included, but is not used here.

Conclusions obtained during the study can be summarized as:

- The spacecraft charging levels generated during single pulse injections are small compared to the beam energy and a pulse will escape the spacecraft loosing only a small fraction of its energy - even in vacuum. During repeated pulsing, the effective current is 0.1 mA, which is small compared to the

thermal electron current to a spacecraft in the ionosphere. Charging rates are expected to be the same as for non-relativistic beams, i.e., to follow the formula *of Parker and Murphy* [1967], with an enhancement factor of 2.5 for low earth orbit spacecraft as demonstrated in the TSS-1R mission [*Thompson et al.*, 1998]. Significant charging (relative to the beam energy) is expected only when the ambient electron density is below $10^9 m^{-3}$.

- Relativistic beams seem to propagate with higher stability than keV beams studied in the past, probably because of the larger beam electron velocity, which reduces space charge effects, and larger relativistic electron mass. Even over-dense beams, where the beam density at injection exceeds the plasma density by several order of magnitudes, propagate well.

- A new phenomenon has been identified for the relativistic regime, which is "ion-focusing", that may be of importance for beam currents over 10 A, but will not affect the linac beam at lower currents. In the ion-focused regime, a beam is partially space charge neutralized. The beam self-forces tend to focus the beam, enhancing the process of pushing ambient electrons out of the beam region, which leads to further beam neutralization.

3.2 Spacecraft Charging

3.2.1 The Plasma Response Time

The spacecraft potential will initially increase with time, causing beam electrons to escape the spacecraft environment with decreasing energy. The ambient plasma will react and attempt to supply an electrically neutralizing return current. In the process, an electric potential sheath is established in the plasma around the spacecraft, causing ambient electrons incident on the sheath edge, to be drawn onto the spacecraft.

In steady-state, the sheath edge is located at a distance from the spacecraft which allows a return current that equals the injected beam current. For ionospheric sounding rockets, the relationship between the beam current and the potential has been found to follow the formula of *Parker and Murphy* [1967],

22

which include effects of ambient magnetic fields [*Myers et al.*, 1989]. Later investigations of data from the NASA TSS-1R mission showed, that the functional dependence between current and potential for LEO satellites also followed Parker and Murphy, but with an enhancement factor of about 2.5, presumably caused by the high orbital motion of LEO spacecraft [*Thompson et al.*, 1998]. The good agreement between theory and experiments was obtained for beams with energies in the few keV-range. The relativistic beams investigated here are not expected to behave any differently, and we conclude based on the work by *Myers et al.* [1989], that significant charging during repeated pulsing of the linac beam will begin only when the ambient density drops below $10^9 \, m^{-3}$.

It is worthwhile pointing out, the beam experiments in space and related beam simulations studies of the past considered beam pulses with pulse lengths of the order of milliseconds or more [*Neubert and Banks*, 1992]. Studying the linac µs-duration pulses corresponds to investigating the beam front in these experiments. The key parameter for the charging state during pulse emissions is the plasma response time τ_p which is of the order of $1/\omega_p$. The ambient plasma density for which $\tau_p = \tau_b$ is approximately $n_p = 2 \times 10^7 \, m^{-3}$. For comparison, f-peak ionospheric densities typically range from 10^{10} (night) to $10^{12} \, m^{-3}$ (day). In the ionosphere, steady state conditions are then expected to be reached during a linac pulse emission. Regions of low plasma density are found both below and above the ionosphere. Below the ionosphere, the beam-spacecraft system is dominated by collisional interactions with the atmosphere, which lead to the creation of a substantial flux of secondary electrons [*Neubert et al.*, 1990], a regime not considered here. However, well above the ionosphere, in the magnetosphere, the plasma density may be so low as to create conditions for the transient state.

From the above discussion, it is clear, that the first parameter to scale properly in the simulation is the ratio of the beam pulse time to the plasma response time, $\tau_{bp} = \tau_b/\tau_p$.

3.2.2 The spacecraft charging rate

A second process to scale properly is the charging experienced by a spacecraft during a pulse injection. The charging rate, if large, may severely affect the beam pulse escape energy from the spacecraft sheath and modify the beam dynamics. The charging rate of a capacitor is:

23

$$\frac{dV}{dt} = \frac{I}{C} \qquad (3.1)$$

where V is the voltage, I the current, and C the capacitance. The capacitance of a conducting sphere with radius r in vacuum is:

$$C = 4\pi\varepsilon_o r \qquad (3.2)$$

With $r = 1$ m and $I = 1$ A, the charging rate is 9 kV μs^{-1}.

Assuming that a 1-m radius sphere is a reasonable approximation of a spacecraft for charging considerations, it follows that the beam system simulated here, with $I_b = 0.1$ A and $\tau_b = 4$ μs, under the transient condition will charge to a maximum of 3.6 kV. The potential energy of electrons on the spacecraft at the end of a pulse injection is then, even in worst case, small relative to the beam accelerator energy, but large relative to the ambient plasma thermal energy. In the simulations, the scaling must be such that the relative magnitude of these entities are maintained.

3.2.3 Scaling of spacecraft charging

To properly compare the simulation world and the real world, one needs to compare the rate of change of the *normalized* potential Φ:

$$\Phi = \frac{qV}{mc^2} \qquad (3.3)$$

With (3.1-3.2), (3.3) becomes

$$\frac{d\Phi}{dt} = \frac{qI}{4\pi\varepsilon_o mc^2 r} \qquad (3.4)$$

The important relationship to establish in the simulation is the number of beam electrons to inject in one time step, such that the electric charging potential energy experienced during one beam pulse injection is small compared to the accelerator energy, but large compared to the ambient plasma energy. The number depends on simulation values of the electron mass and charge and the number density of the ambient plasma.

The beam current at the accelerator can be given in terms of the number of electrons ejected per unit time N_a':

$$I_b = qN_a'$$ (3.5)

With (3.4-3.5), the charging state can now be described by:

$$\Delta\Phi = \frac{q^2N_a'}{4\pi\varepsilon_o mrc^2}\Delta t$$ (3.6)

or:

$$\Delta\Phi = \frac{N_a'}{4\pi n_p rc^2\tau^2_p}\Delta t$$ (3.7)

For $\Delta t = \alpha\tau_b$, where α is the fraction of a beam pulse injected, we can write the charging state as:

$$\Delta\Phi = \frac{N_a'}{4\pi n_p rc^2}\alpha\frac{\tau_{bp}}{\tau_p}$$ (3.8)

Equation 3.8 is used for deciding on the simulation parameters. The simulation domain is on a 3D grid with grid-spacing $\Delta=1$, and time step $\Delta t = 1$. The velocity of light, $c = 0.5$, such that a relativistic electron will move approximately 0.5Δ in one time step. The first simulation grid used is 256Δ x 128Δ x 128Δ, with the beam pulse propagating in the positive x-direction.

The spacecraft is as a cube of size 10Δ x 10Δ x 10Δ, centered in y and z and at $x = 64\Delta$, such that the approximate equivalent spherical spacecraft radius is $r = 5$. For simulations of a complete beam pulse ($\alpha = 1$), the beam pulse duration is chosen to be 250 Δt, which allows both the head and tail of the pulse to be resolved properly. The ambient simulation density is $n = 1$ for the steady state conditions, which is a low number to reduce computational effort, but not to low to resolve kinetic plasma effects. The transient state, where no significant return currents are generated during the time of the pulse injection, will be simulated using injection into a vacuum.

For steady-state, we chose a plasma with approximately five ambient plasma periods during one beam pulse injection, or more specifically, $\tau_b/T_p = 5.17$, giving $\tau_{bp} = 32.5$. In the simulation, ions are

assumed stationary. With the code employed, one need not include ions at all in this case, thus further reducing the computational load.

With these numbers, (3.8) becomes:

$$\Delta\Phi = \alpha \frac{N_a{}'}{3.72}$$

(3.9)

When deciding on the beam particle injection rate, the requirement is to maintain the relative ordering of normalized plasma energy, beam energy and final spacecraft electric potential energy for vacuum. From (3.9) we conclude that 10 electrons pr. time step seems a reasonable injection rate. With a beam cross section at injection in the simulations of $4\Delta^2$ and a simulation velocity of 0.5, the beam density at injection is then 5, or 5 times the ambient density ($n_b{}''/n_p=5$). The normalized energies for $N_a{}' = 10$ is shown in Table 3.2. With our choice of parameters, the relative order is maintained in the simulation. However, the escape energy in vacuum will be reduced to 7.1, which is more than in the real world. As will be clear from the simulations, this is not a problem for the physics under investigation.

Table 3.2: *normalized energies representative for an experiment in the ionosphere and in the simulation*

	real world	simulation
plasma energy	10^{-7}	2×10^{-3}
beam energy	9.8	9.8
S/C potential	0.007	2.7

3.2.4 Test of Spacecraft Charging Rates

The scaling law and the implementation of a spacecraft in the simulation has been tested by injection of a beam into a vacuum with the parameters given in the past subsection. The normalized potential of the spacecraft is determined each time step by integrating the radial electric field component along y from the $y=0$-boundary and to the center of the spacecraft. Particles hitting the spacecraft are arrested and written

off, and electric fields from surplus charge are conducted freely within the spacecraft structure. Thus, charge from the accelerator is redistributed with the speed of light within the structure.

Figure 3.1 shows the spacecraft potential as a function of time (full line) and the corresponding analytical prediction for vacuum given by (3.4) (dashed line). On the top is shown the vacuum case and on the bottom the plasma case. The electric field forming around the spacecraft and the injected beam is being established with the speed of light. The charging of the spacecraft is thus lagging the analytical estimate. However, the charging rates for vacuum shown on the left compare very well, and the spacecraft retains it potential after termination of pulse injection (not shown). For injection into a plasma ($n_b{}^o/n_p$=5), the spacecraft is clearly well neutralized by the plasma current. The time scale is sown in units of the plasma period for the plasma case on the bottom panel.

Thus, we are satisfied, that the incorporation of a spacecraft and accelerator into the TRISTAN code is done properly, and that the correct scaling laws between the real world and the simulation world have been identified.

3.3 Beam Dynamics

3.3.1 A First Look at Beam Dynamics

A first cut at simulations of a complete beam pulse is done with the parameters given in the previous section for the transient condition with injection into a vacuum and for the steady state conditions with τ_{bp} = 5.17 ($n_b{}^o/n_p$=5). Results are given at a point just after the beam is turned off at t = 256Δt, where the beam pulse has been injected in the interval t = 0-250Δt. Figure 3.2 shows the position and the energy of the beam electrons for the vacuum case (left) and the ambient plasma case (right). The beam has been injected at 45° pitch angle with 8° angular spread. The non-relativistic gyro frequency equals the non-relativistic plasma frequency for the plasma case.
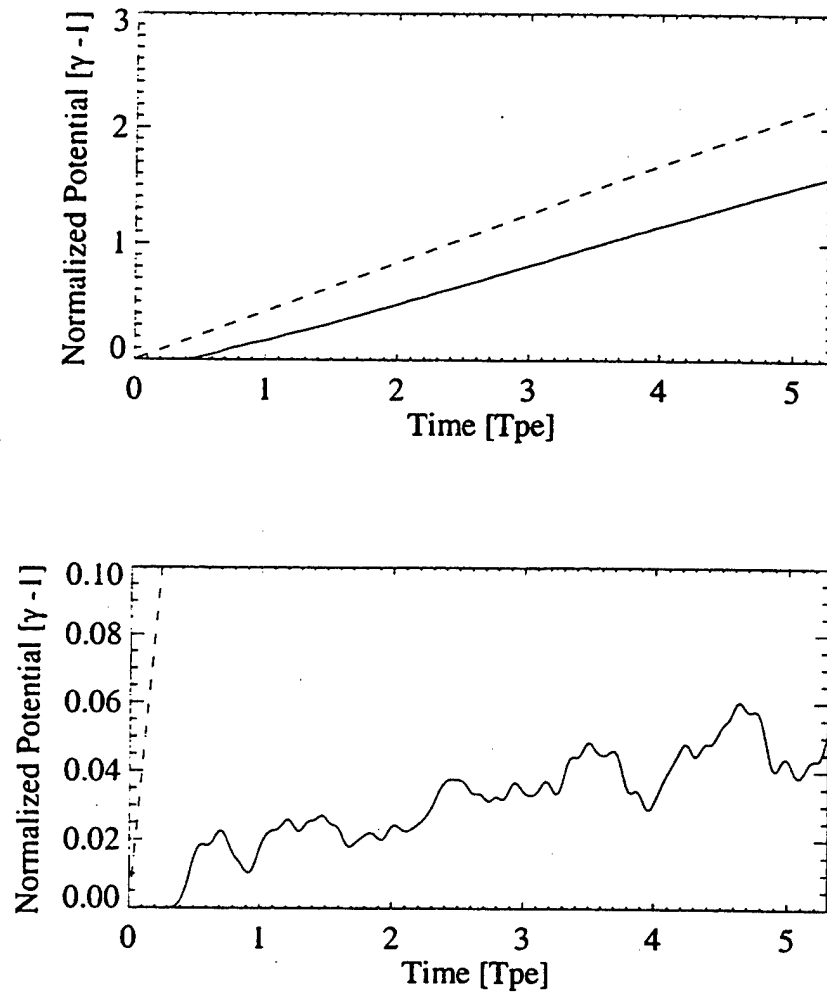
Figure 3.1:   Spacecraft potential as a function of time. **Top**: beam into vacuum; **Bottom**: beam into plasma ($n_b{}^o/n_p$=5). **Full line**: simulation, **dashed line**: vacuum theory (equation 3.4). Time is measured in plasma periods for the plasma case.

Figure 3.2: Beam position and energy at $t=256\Delta t$ ($t/T_{pe}=5.2$ for the plasma case). Beam injection pitch angle $\theta = 45°$ with angular spread $\Delta\theta = 8°$; beam density at injection. **Left**: beam into vacuum; **right**: beam into plasma ($n_b^o/n_p = 5$). An ambient magnetic field is directed along the x-axis.

Looking first at the beam position, it is noted, that the beam in vacuum has undergone significant radial expansion, which primarily is due to the initial spread in the beam injection angle, while in the plasma case the beam is mu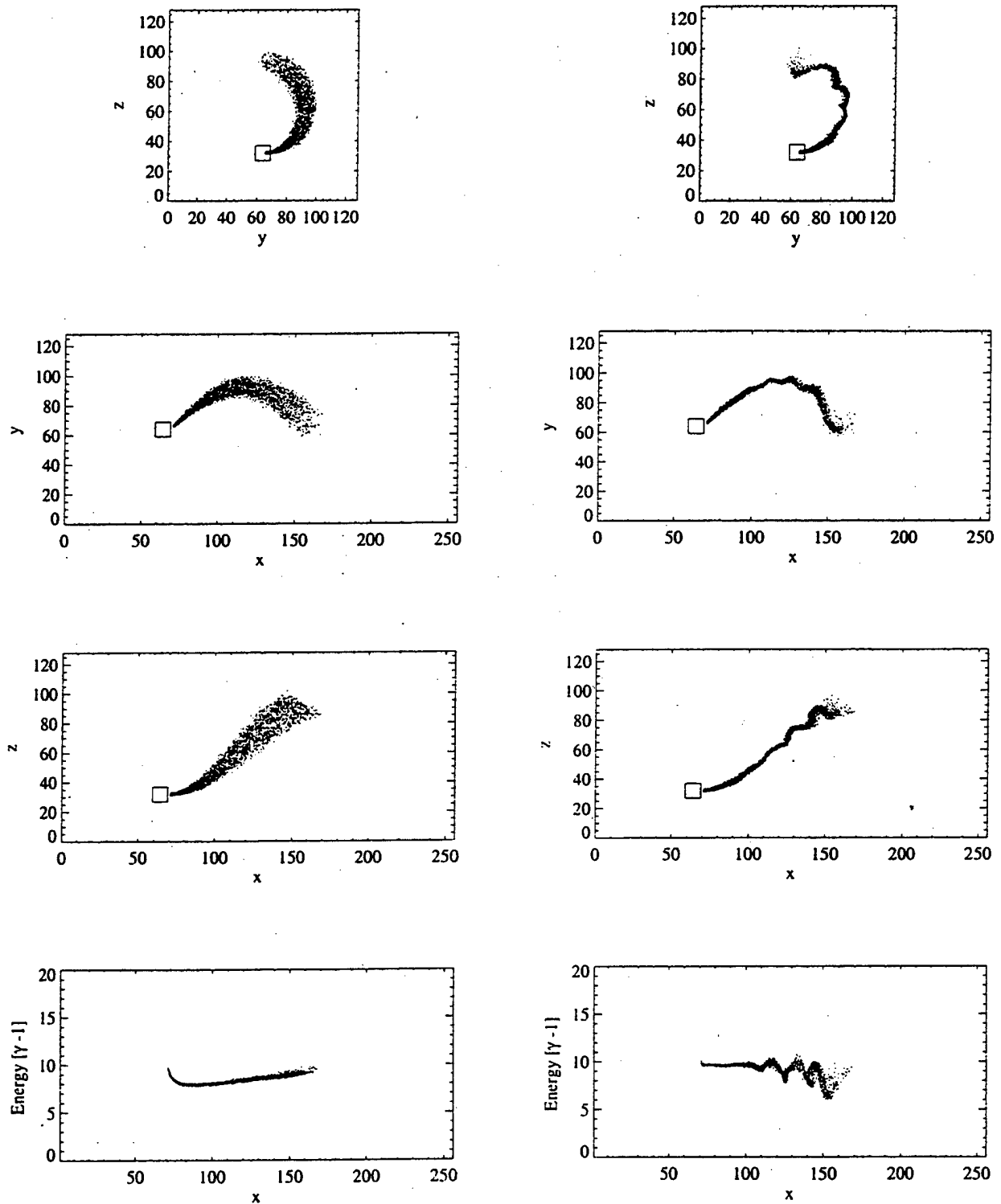ch more focused. From the plots of beam energy as a function of position, it is clear, that in the vacuum case, the beam experiences a gradual decrease in energy, which corresponds to the loss of escape energy because of spacecraft charging consistent with the charging shown in Figure 3.1 (top), for the same simulation parameters. The energy loss is smooth and the beam pulse undergoes no unstable oscillations. In the plasma case it is clear that the beam pulse is subject to strong oscillations, leading both to higher and much lower energies than the injection energy. The oscillations grow with time in the plasma, being more severe in the front of the pulse than in the rear. It is also seen from the tail of the pulse, that the escape energy in the plasma is close to the accelerator energy, i.e., the spacecraft is well neutralized.

Because the beam density relative to the ambient density clearly is an important parameter, we must look more closely at the injection process, and carefully simulate the beam radial expansion process. But first we take a look at an useful analytical description of the beam expansion problem.

3.3.2 The Paraxial Envelope Equation

The radial expansion of the beam is described by the paraxial envelope equations [Lawson, 1988, Humphries, 1990]. Considering only terms relevant for the present problem of a relativistic electron beam in a magnetic field, the equations reduce to:

$$a'' = \frac{K}{a} + \frac{\varepsilon^2}{a^3} - \frac{\Omega_L^2}{\beta^2 c^2} a \qquad (3.10)$$
$$\quad\ (1)\quad\ (2)\quad\ (3)$$

where a'' is the second derivative of the beam radius with respect to the distance along the beam axis, and Ω_L is the beam electron Larmor frequency ($=-qB/2\gamma m_o$). K is the generalized perveance:

$$K = \frac{2I}{\beta^3 \gamma} \left[\frac{1}{\gamma^2} - f_e \right] \qquad (3.11)$$

where the normalized current $I=I_b/I_o$ and:

$$I_o = \frac{4\pi\varepsilon_o m_o c^3}{q} \quad (= 17000 \text{ A}) \tag{3.12}$$

The perveance is the sum of beam-generated forces from the non-neutralized space charge within the beam, that attempts to expand the beam, and the beam self magnetic field, which tends to contract the beam. The parameter f is the degree of beam charge neutralization by the ambient plasma, and it takes on values between 0 and 1. A completely charge neutralized beam will have $f=1$, in which case K is negative. It is interesting to look at the perveance values in the limits $f=0,1$ for non-relativistic ($\gamma=1$) and relativistic ($\beta=1$) beams. At these limits we have:

$$-2I \leq K \leq 2I/\beta^2 \quad \text{non-relativistic} \tag{3.13}$$

$$-2I/\gamma \leq K \leq 2I/\gamma^3 \quad \text{relativistic} \tag{3.14}$$

For non-relativistic beams, K is likely to be positive, while for relativistic beams, K will often be negative. From (3.10), one can see that the sign of K is important for the propagation characteristics. Even with no ambient magnetic field, relativistic beams with K negative have the possibility of propagation with the radius maintained below a maximum value. In this case, the positive emittance term balances the negative perveance term. Moving from non-relativistic beams to relativistic ones, one then has to consider the new phenomena *of beam propagation in the ion-focused regime.*

3.3.3 Simulation of Radial Expansion

The radial expansion of the beam is very important to understand because the stability of the beam depends on the ratio of the beam and the ambient plasma density. For low beam density, the interaction is weak. To better understand the relative importance of the three terms in the envelope equation, and to help assure that they are scaled properly to the simulations, values of the terms at injection are computed for a range of beam currents and shown in Table 3.3. The table shows values of the perveance term for f = 0 (K_o) and for f = 1 (K_I). First it is noted, that at injection, the emittance term (2) dominates. It can be shown, that initially, the beam expands with the emittance angle $\Theta_\varepsilon = \varepsilon/a_o$. In case of a charge neutralized beam, the next term to dominate when the radius increases is the perveance term. Finally, if the beam

continues to expand, the ambient magnetic field will eventually bring the radius back in again. The last columns show the radii where the magnitude of the terms equal each other.

The current values shown in the table range from the beam current of 0.1 A and to 100 A. As will be shown later, it is only for the highest values, that ion-focusing may become an issue, at least predicted by the envelope equations. With the range shown, we thus explore the regime from below to above the currents, where this may become an issue in a space experiment, and compare these analytical predictions with simulations, where plasma kinetic effects are accounted for. An important issue here is to what extent a beam is space charge neutralized. This is what a particle code can elucidate.

Table 3.3: Magnitude of terms in Equation 3.10 at injection in ionosphere and in simulation.

Real world	0: $K0/ao$	1: $K1/ao$	2: ε^2/ao^3	3: $(\Omega L^2/\beta^2 c^2) ao$	a/ao 1=2	a/ao 1=3	a/ao 2=3
Ib = 0.1 A	6.3×10^{-6}	-7.3×10^{-4}	9.6	3.6×10^{-9}	114	449	227
Ib = 1.0 A	6.3×10^{-5}	-7.3×10^{-3}	9.6	3.6×10^{-9}	36	1418	227
Ib = 10.0 A	6.3×10^{-4}	-7.3×10^{-2}	9.6	3.6×10^{-9}	11	4485	227
Ib = 100.0 A	6.3×10^{-3}	-7.3×10^{-1}	9.6	3.6×10^{-9}	3.6	14183	227
simulation							
N$^+$=10 vacuum	1.1×10^{-6}	-	1.7×10^{-2}	1.2×10^{-4}	-	-	3.4
N$^+$=10 plasma	1.1×10^{-5}	-1.2×10^{-3}	1.7×10^{-2}	1.2×10^{-4}	3.7	3.1	3.4
N$^+$=100 plasma	1.1×10^{-4}	-1.2×10^{-2}	1.7×10^{-2}	1.2×10^{-4}	1.2	10	3.4

To simulate the radial expansion of the beam, injection is at $0°$ pitch angle along x. This allows a smaller dimension perpendicular to the beam and the ambient magnetic field, and the simulation domain is now $1024\Delta \times 64 \Delta \times 64 \Delta$. The pulse length is now 4 times as long (1000 Δt) and the electric charge one quarter of the one used previously, such that one pulse length still equals 5.17 *Tpe* for the plasma cases. The gyro radius is maintained unchanged to limit the radial excursions, and thus the gyro frequency is 4 times the one previously used.

The terms of the paraxial envelope equation for the simulations are also shown in Table 3.3. In the simulation, the emittance term also dominates, except for the highest current values investigated. The perveance terms scale almost directly between the real world and the simulation world. The emittance terms are generally smaller in the simulations because it is impossible to completely resolve a small beam

radius and at the same time contain a full pulse length within the simulation domain. Recall, that the beam radius is 1.5 mm, and the pulse length is 1.2 km. In the simulation, the radius is therefore relatively larger than in the real world. The ambient magnetic field term (3) is also the smallest in the simulation, except for the lowest current case.

Equation 3.10 has been solved numerically with the real world current values of Table 3.3 and results are shown in Figure 3.3. On the top is shown normalized radius as a function of distance along the beam for the various current cases and on the bottom the same for the simulated currents. The thick line represents the solutions for all current cases with $K=K_0$, and for the lowest current cases for $K=K_1$. For these situations the perveance term is so small as to have no impact on the solution. Only as currents increase, does the perveance term begin to influence the solution, but only for the case of a charge-neutral beam ($K=K_1$). For the real beam, the 1.2 km pulse length is shown in a typical ionospheric magnetic field, which corresponds to about 0.5 of a oscillation. For the simulation, the magnetic field is relatively higher, and about 3.5 oscillations are shown for the cases represented by the thick curve. Figure 3.3 demonstrates that the simulations also cover the transition region from low currents, where the perveance term is unimportant, to the high current region, where ion-focusing may become important.

Simulation results are shown in Figures 3.4-3.6 for beam in vacuum ($n_b^o=1$), and beams in plasma ($n_b^o/n_p =5, 50$). On the left panels, the beam electron positions (top) and energies (bottom) are shown just after the end of the beam pulse emission at $t/T_{pe}=5.3$ and on the right panels at $t/T_{pe}=8.4$. On the plots of the beam electron positions, the solutions to 3.10 are shown for $K=K_0$ (top curves) and $K=K_1$ (bottom curves) (for the vacuum case both curves are for $K=K_0$ as the beam must be completely non-neutralized). The beam envelope modulation seen in the simulations and the analytical solutions for a non-neutralized beam are in very good agreement in the first 2 figures, and mainly reflects the gyration of electrons in the presence of the ambient magnetic field. In the last case shown in Figure 3.6, however, the picture becomes much more complex. This is also the case, where a negative perveance may play a significant role. This term pinches portions of the beam front enough to push the ambient electrons aside, and allow segments of the beam to propagate as partially charge neutralized. At the same time, the beam

33

is undergoing strong beam-plasma interactions with spatial modulation lengths that are shorter than predicted by 3.10. The results indicate, that while the analytical considerations point to the beam forces as instrumental in establishing conditions for beam pinching and propagation in the ion focused regime, beam-plasma interactions dominate the propagation aspects by establishing more complicated plasma structures in the beam region, which in turn determines a rather complicated functional dependence of the parameter f with space and time.
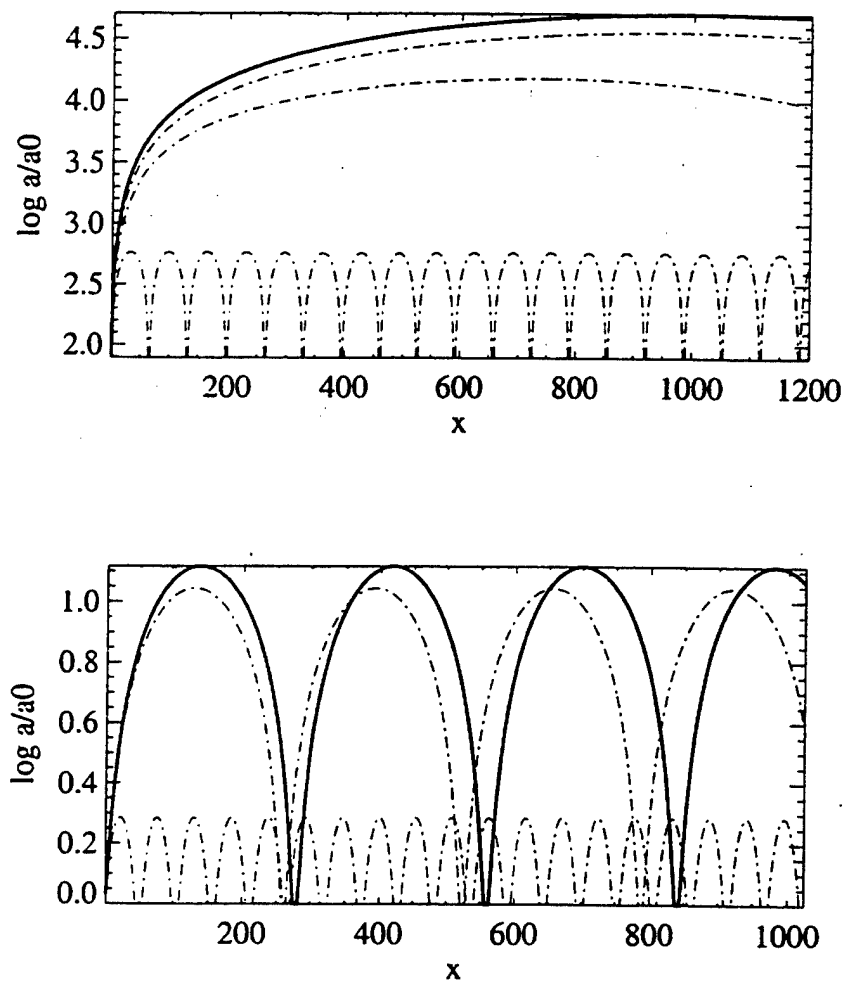

Figure 3.3: Beam envelopes for different beam currents. **Top**: real beams, $I_b = 1, 30, 60, 100$ A. Thick curve is for non-neutralized beams, where K_0 is small for current values investigated, as well as for neutralized beam at the lowest current, where K_I is also small. Dashed curves are for neutralized beams, where increased currents have increased pinching effect on beam. **Bottom**: same for simulated beams with $N'=1, 10, 100$. For real beams (top), distance along beam (x) shown corresponds to length of a 4 μs-beam. Envelope of thick curve represents magnetic field focusing and distance shown corresponds to app. 0.5 oscillation length. In simulation, a relatively higher magnetic field is chosen to limit beam radius. Here, thick curve traces approximately 3.5 magnetic field-induced oscillations.
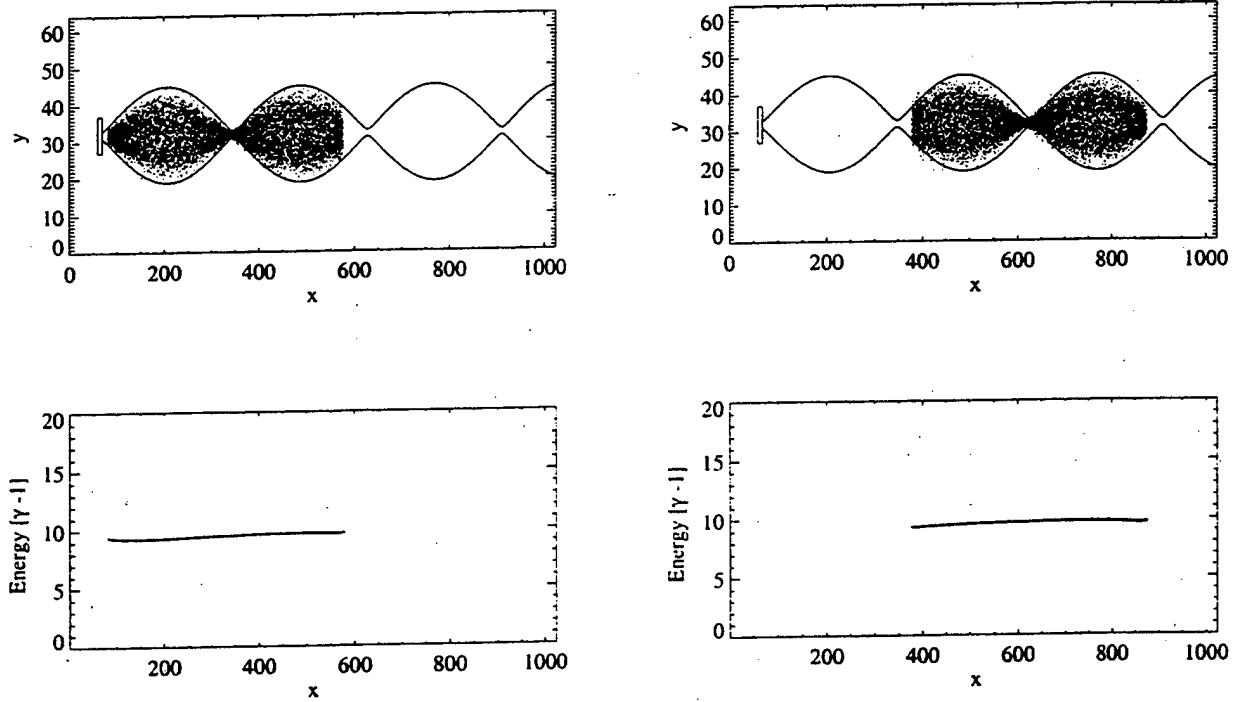
34

Figure 3.4: Beam in vacuum with magnetic field directed along x. Beam density is $n_b{}^\circ=5$, magnetic field $\Omega_l\Delta t=5.6\times10^{-3}$, and beam pitch angle at injection $\theta = 0^\circ$, with $\Delta\theta = 8^\circ$. Beam pulse length $\tau_b=1000\Delta t$. **Left:** $t=1024\Delta t$; **Right:** $t=1624\Delta t$. **Top:** beam position in the xy-plane. Horizontal scale is highly compressed as seen in distortion of spacecraft. Full curve is solution to beam envelope Equation 3.10 for non-neutralized ($f=0$) beam; **Bottom:** normalized beam energy as a function of x.
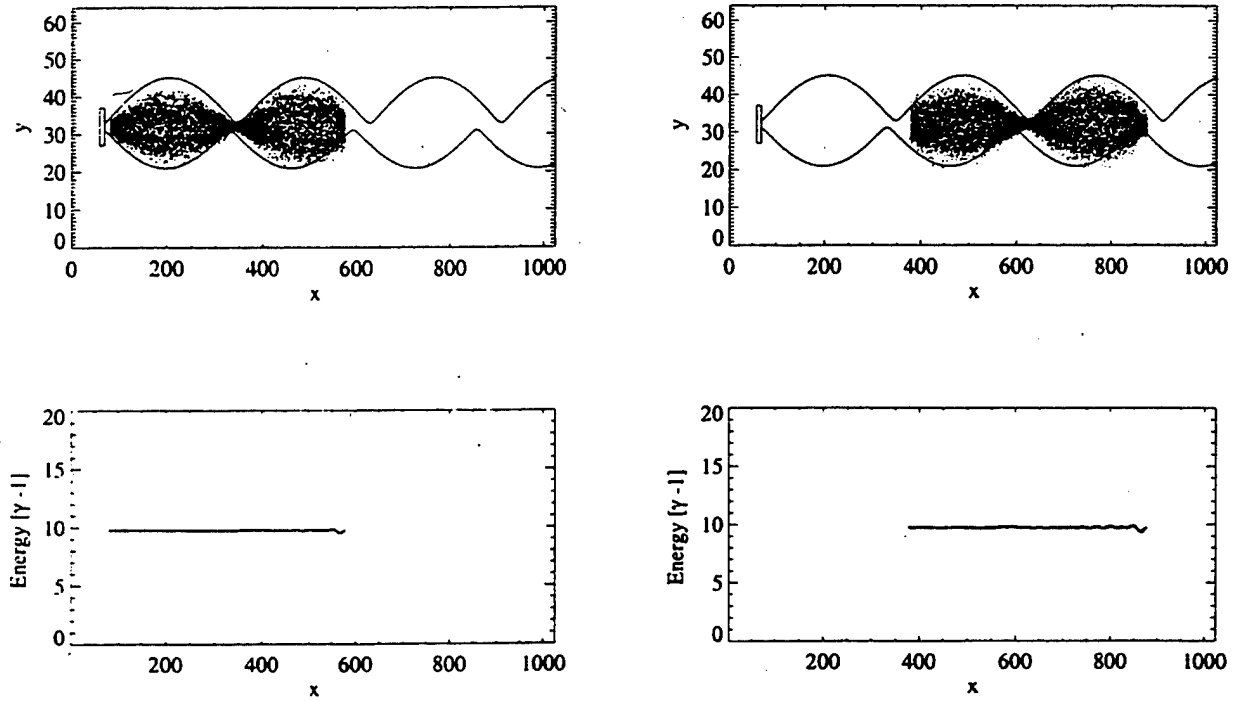
Figure 3.5: Beam into plasma ($n_h{}^o/n_p$=5) with a magnetic field directed along the x-axis ($\Omega_L \Delta t$=5.6x10^{-3}). Beam pitch angle at injection $\theta = 0°$, with $\Delta\theta = 8°$. Beam pulse length τ_b= 1000Δt. **Left**: t=1024Δt (t/T_{pe} = 5.3); **right**: t=1624Δt (t/T_{pe} = 8.4). **Top**: beam position in xy-plane; **bottom**: beam energy as a function of x. Full curve is solution to beam envelope Equation 3.10 for non-neutralized (f=0, top curve) and neutralized (f=1, bottom curve) beam.
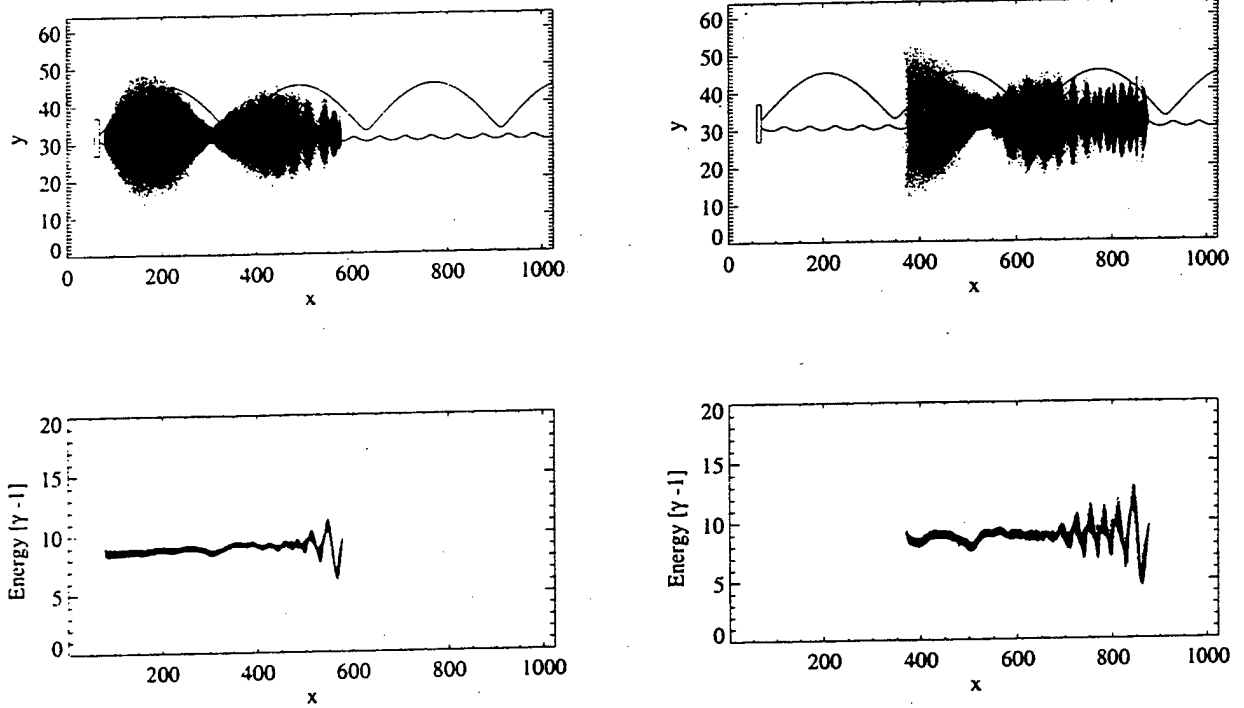
Figure 3.6: Beam into plasma ($n_b{}^o/n_p$=50) with a magnetic field directed along the x-axis ($\Omega_L\Delta t$=5.6x10^{-3}). Beam pitch angle at injection $\theta = 0^\circ$, with $\Delta\theta = 8^\circ$. Beam pulse length τ_b= 1000Δt. **Left**: t=1024Δt (t/T_{pe} = 5.3); **right**: t=1624Δt (t/T_{pe} = 8.4). **Top**: beam position in xy-plane; **bottom**: beam energy as a function of x. Full curve is solution to beam envelope Equation (3.10) for non-neutralized (f=0, top curve) and neutralized (f=1, bottom curve) beam.

To expand further on this point, Figure 3.7 shows the electron density along the x-axis through the center of the beam as a function of time. On the left plots are shown the case of $n_b{}^o/n_p$ =5 and on the right $n_b{}''/n_p$ =50. Top plots are the beam densities, and bottom plots the ambient densities. The plasma is pushed out of the beam region at the nodes, where the electrons after one gyration concentrate in a small region with high density. When the beam density is lower, the effect is minor, an influences on the beam are small. For higher values of the density, the effect of the beam is much stronger, and changes in ambient plasma conditions in the beam region has a severe effect on beam propagation. One can probably consider this a transient stage, where a channel is being formed in the plasma allowing later portions of the beam to propagate with much smaller energy loss.
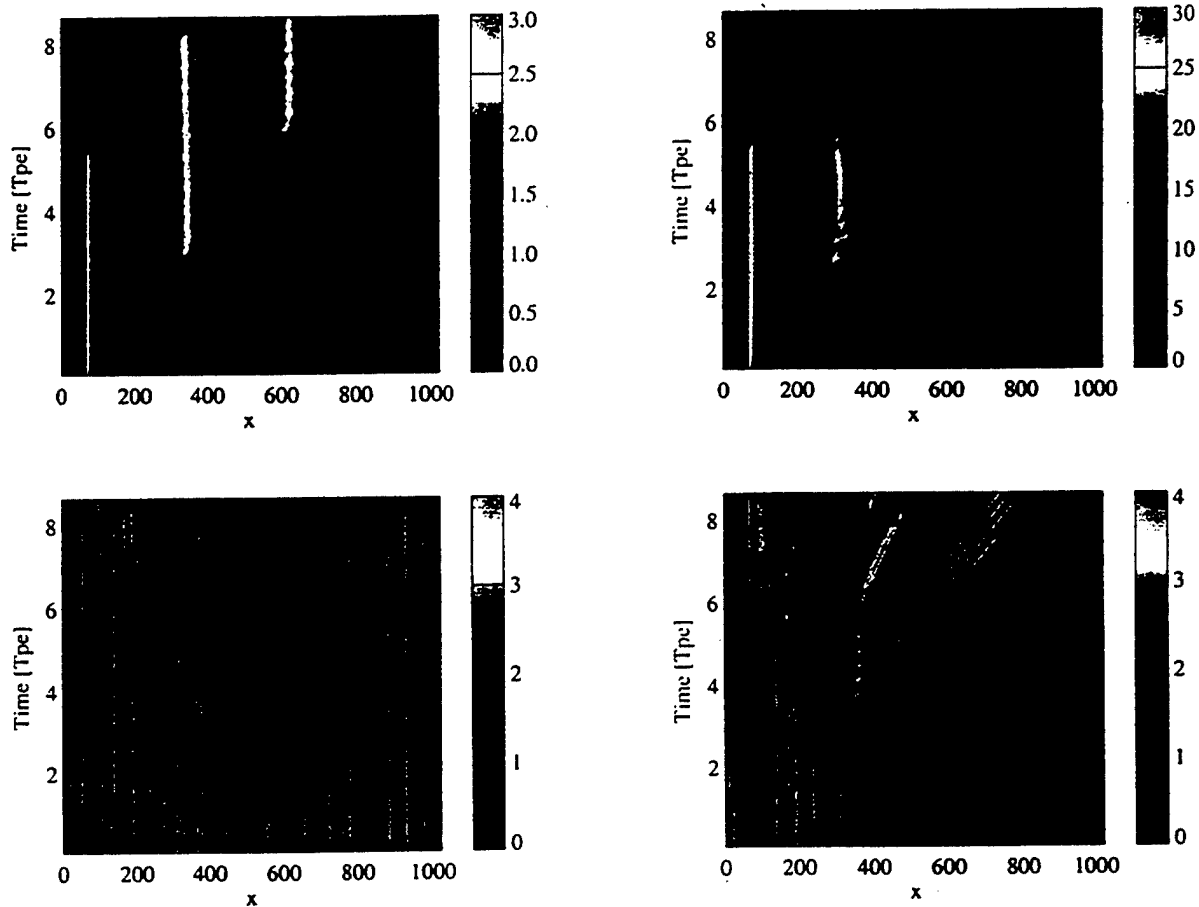
Figure 3.7:   Beam and plasma densities on the x-axis as a function of time. **Left:** $n_b{}^o/n_p=5$; **right** $n_b{}^o/n_p=50$. **Top:** beam; **bottom:** plasma.

3.4 PIC Summary

Spacecraft charging effects have been considered looking towards experiences with keV beams, as the principles of charging are not expected to depend on beam energy. Charging effects are expected only for ambient densities below 10^9 m^{-3}.

Beam dynamics is known to depend critically on beam-to-ambient plasma densities, and thus the radial expansion of a beam is of primary interest. The question is, will a beam, injected with a high density, expand to low densities before significant beam-plasma interactions take place? Our results indicate, that for the currents considered for the linac beam, there will be no problem at least within several 10's of km of the injection point. For higher current beams, where ion-focusing plays a role (above 10 A), beams will attempt to form an ion channel in the plasma and will expend some energy in this process. For the

38

short pulses considered here, a significant, if not all of the beam pulse, will be involved in this process, while for ms-duration beams, a larger portion of the beam may propagate relatively stable in the ion-channel formed by the beam front.

For longer distance propagation, the beam will experience scattering in both energy and pitch angle. Upward injection from the ionosphere will result in a significant portion of the beam being scattered out of the loss cone, to form curtains of energetic electrons drifting around the Earth like radiation belt electrons. Estimates of energy loss in the process is of the order of 10% or less, a number found for relativistic electrons injected into the magnetosphere from above thunderstorms during Sprite generation [*Lehtinen* et al., 2000]. For beam injection downwards into the upper atmosphere from the ionosphere, a situation of interest when studying properties of artificial upward discharges, only a small fraction of the beam energy will be lost to beam-plasma interactions.

4. Time Dependent Relativistic Electron Beam Distribution Simulations in the Ionosphere-Magnetosphere: Khazanov4D and Khazanov5D Models

This task was accomplished by updating time-dependent, field-aligned kinetic models of electron transport [*Khazanov et al.*, 1994] for relativistic energies and interactions. Two models were revised and applied to the present situation. The first is a 4D model (one space, 2 velocity space, and one time) which we refer to here as the Khazanov4D model. A second model, with gyration- and bounce-averaging, referred to here as the Khazanov5D model [*Khazanov et al.*, 1996], was also extended to relativistic energies and waves were included in the model.

The following summarizes the study of relativistic electron beam injection simulations being conducted with the Khazanov4D and Khazanov 5D plasma transport models.

4.1. Theory and Cross Section Discussion

In the Khazanov4D model, a gyration-averaged approach is assumed because the electron cyclotron period is by far the smallest time scale under consideration. In this limit, the field-aligned kinetic equation becomes

$$\frac{1}{v}\frac{\partial\phi}{\partial t} + \mu\frac{\partial\phi}{\partial s} - \frac{1-\mu^2}{2B}\frac{\partial B}{\partial s}\frac{\partial\phi}{\partial\mu} = \langle S\rangle + Q \tag{4.1}$$

where ϕ is the flux of electrons in units of $cm^{-2}s^{-1}eV^{-1}sr^{-1}$, E is the kinetic energy of the electron and $\mu=\cos\theta$. Field-aligned forces have also been omitted from this equation, because it is expected that there will be no parallel forces significant enough to alter the relativistic electron trajectory. The left-hand side of (4.1) represents collisionless transport along the geomagnetic field, while the right-hand side represents all collisional processes by $\langle S\rangle$ and sources by Q. Using a continuous loss approximation, the atmospheric electron-neutral interactions within $\langle S\rangle$ have the form

$$\langle S_{e\alpha}^0\rangle = \sum_\alpha \frac{n_\alpha\sigma_\alpha^{(1)}}{2}\frac{\partial}{\partial\mu}\left[(1-\mu^2)\frac{\partial\phi}{\partial\mu}\right] \tag{4.2}$$

$$\langle S_{e\alpha}^+\rangle = \sum_\alpha n_\alpha\sum_r \frac{\partial}{\partial E}\left\{\left(E_{\alpha r}^+ + \langle E_s\rangle_{\alpha r}\right)\sigma_{\alpha r}^+\phi\right\} \tag{4.3}$$

Equation (4.2) represents elastic scattering with each atmospheric neutral species α, where $\sigma_\alpha^{(1)}$ is the momentum transfer cross section,

$$\sigma_\alpha^{(1)} = \int I_\alpha(E,\chi)(1-\cos\chi)d\Omega \tag{4.4}$$

where I_α is the Moliere elastic cross section discussed in previous reports and χ is the scattering angle. In (4.3), $\sigma_{\alpha r}^+$ is the total ionization cross section for species α into ionization state r calculated by integrating $I_{\alpha r}^+(E,E')$, the Møller inelastic cross section discussed in previous reports, over the secondary electron energies E', $E_{\alpha r}^+$ is the ionization potential, and $\langle E_s\rangle_{\alpha r}$ is the average energy of the secondary electron spectrum,

$$\langle E_s \rangle_{ar} = \frac{1}{\sigma_{ar}^+} \int E' T_{ar}^+ (E, E') dE' \qquad (4.5)$$

Also, excitation collisions are neglected because the cross sections are vastly smaller than the ionization cross sections. Therefore, the collisions of relativistic electrons with atmospheric neutral particles can be reduced to two lookup tables for $\sigma_\alpha^{(1)}$ and $\sum_r \left(E_{ar}^+ + \langle E_s \rangle_{ar} \right) \sigma_{ar}^+$, both of which are functions of the atmospheric constituent and the electron energy. The first quantity is the momentum transfer cross section, and the second quantity we will call an energy-loss cross section, with units of $eVcm^2$.

We will begin our calculations with only the three principal atmospheric species included in the calculations: O, O_2, and N_2. The momentum transfer cross sections, from (4.4), for these species are shown in Figure 4.1.

The calculation of the second term is not so straight-forward, because information must be known about the ionization potentials and kinetic energies of each electron in the atmospheric constituent. First, let us examine the dependence of the cross section on the kinetic energy of the target electron (that is, the electron to be expelled from the cloud surrounding the nucleus).

Figure 4.2 shows results for a binding energy of 13.6 eV and four values of the target electron kinetic energy: 0.01 eV, 1 eV, 13.6 eV, and 150 eV. As seen in this figure, there is very little dependence of the cross section on the kinetic energy of the target electron. In principal, these kinetic energies can be calculated theoretically because it is primarily dependent on the velocity required to maintain an orbit around the nucleus, but the cross-electron interactions make the calculations prohibitively cumbersome, and they are not critical to the result in any case. Therefore, the kinetic energy will be taken as equal to the ionization energy for that target electron.

Uncertainty is still found in the choice of binding energy, however, and also in the number of target electrons associated with each ionization potential. Test cases have shown, though, that this is much less of a problem than expected because the inner shell electrons with ionization energies more than an order of magnitude larger than the outer shell energies have cross sections far below the outer shell results. This is seen in Figure 4.3, where ionization values of 15 eV, 300 eV, 1000 eV, and 1500 eV have been used. It is clear that only the ionization of the outer shell will significantly contribute to the total cross section, particularly for relativistic energies, even when the inner shell cross sections are multiplied by the number of target electrons in these shells.
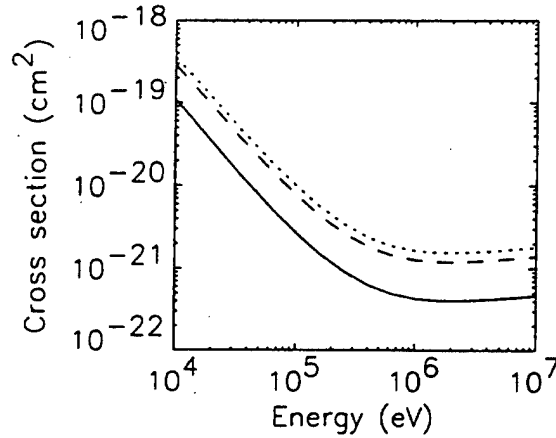
Figure 4.1: Moliere momentum transfer cross sections for O (solid line), O_2 (dotted line), and N_2 (dashed line).
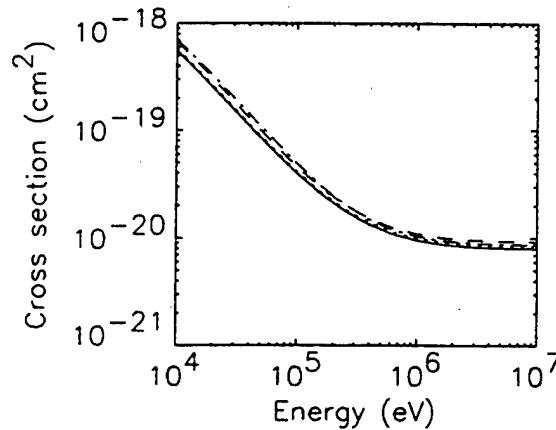

Figure 4.2: Inelastic cross sections for 13.6 eV ionization energy with target electron kinetic energies of .01 eV (solid line), 1 eV (dotted line), 13.6 eV (dashed line), and 150 eV (dash-dot line).

It is also clear to see from Figure 4.3 how sensitive the cross section is to the choice of the ionization energy. This sensitivity indicates that it is appropriate to take into account the various excitation states in which the newly created ion can be left. Values for these ionization potentials, and the corresponding branching ratios for each, are given in Table 4.1. These values are from the non-relativistic ionization potentials given by *Jackman et al.* [1977]. The branching ratios were determined from the high-energy range of the validity of these cross sections, and are multiplied by the number of electrons in the outer shell of each constituent, taken as 2, 4, and 4 for the three species of interest (O, O_2, and N_2, respectively).
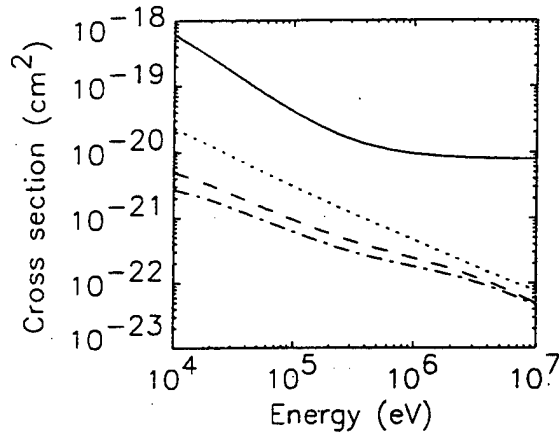
Figure 4.3: Inelastic cross sections with ionization energies of 15 eV (solid line), 300 eV (dotted line), 1000 eV (dashed line), and 1500 eV (dash-dot line).

Table 4.1: Ionization states and branching ratios

O states	E^+	Ratio	O_2 states	E^+	Ratio	N_2 states	E^+	Ratio
^4S	13.60	.370	X	12.10	.079	X	15.58	.456
^2D	16.90	.410	a	16.10	.191	A	16.73	.200
^2P	18.50	.210	A	16.90	.191	B	18.75	.104
			b	18.20	.170	D	22.00	.070
			B	20.00	.110	C	23.60	.070
			c	23.00	.160	40	40.00	.100
			37	37.00	.099			

Cross section results, along with the average secondary electron energy from (4.5) and the total "energy-loss cross section," are presented in Figures 4.4-4.6. In the cross section plots (top panels), the solid line is the summation of the partial cross sections for each ionization state. Note that these cross sections are integrated over the range of secondary electrons, and that all three species have a cross section of about 2×10^{-20} cm^2 for relativistic primary energies. The middle panels show the average secondary electron energies for each ionization state, and the solid line is a weighted average,

$$\langle \bar{S}_e \rangle_\alpha = \frac{\sum_r \sigma_{\alpha r}^+ \langle S_e \rangle_{\alpha r}}{\sum_r \sigma_{\alpha r}^+} \tag{4.6}$$

It is interesting that the average secondary energy from a relativistic primary energy is about 300 eV, while the average secondary in the non-relativistic limit is about 20 eV. In the lower panel, the solid line is the result from summing the various ionization states while the dotted line is the result with all of the newly created ions starting in the ground state. These results show that assuming all of the outer

43

shell electron ionizations jump to the ground state of the ionized particle is valid, and that using this table of branching ratios into the various ionization states is merely fine-tuning to the overall quantity needed in the model.
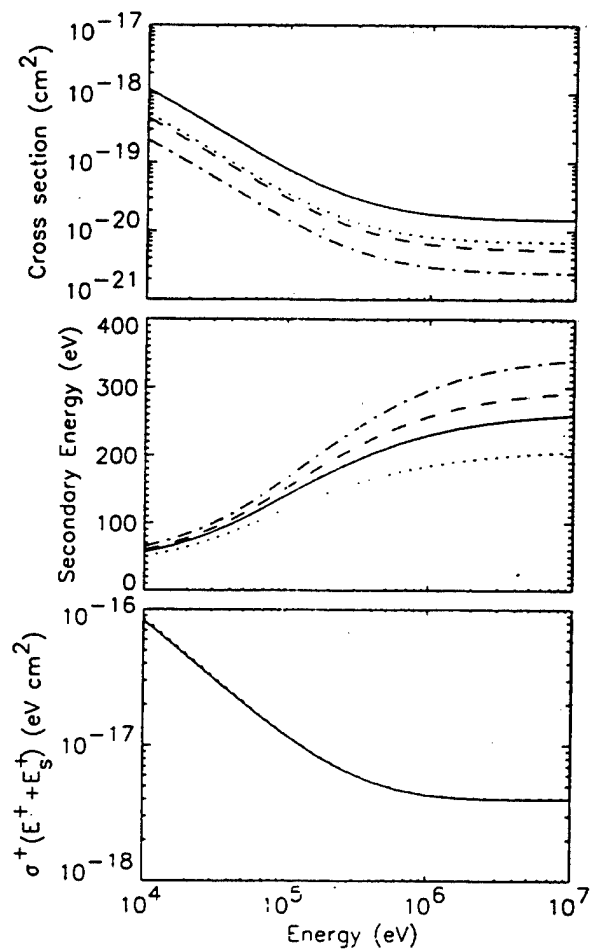

Figure 4.4: Cross sections, average secondary energies, and total energy-loss cross section for atomic oxygen.
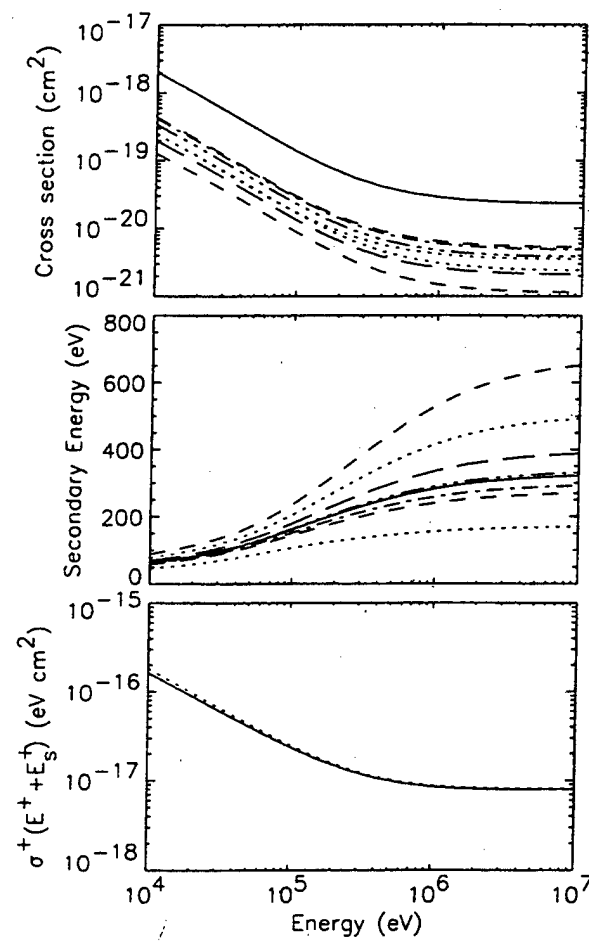
Figure 4.5: Cross sections, average secondary energies, and total energy-loss cross section for molecular oxygen.
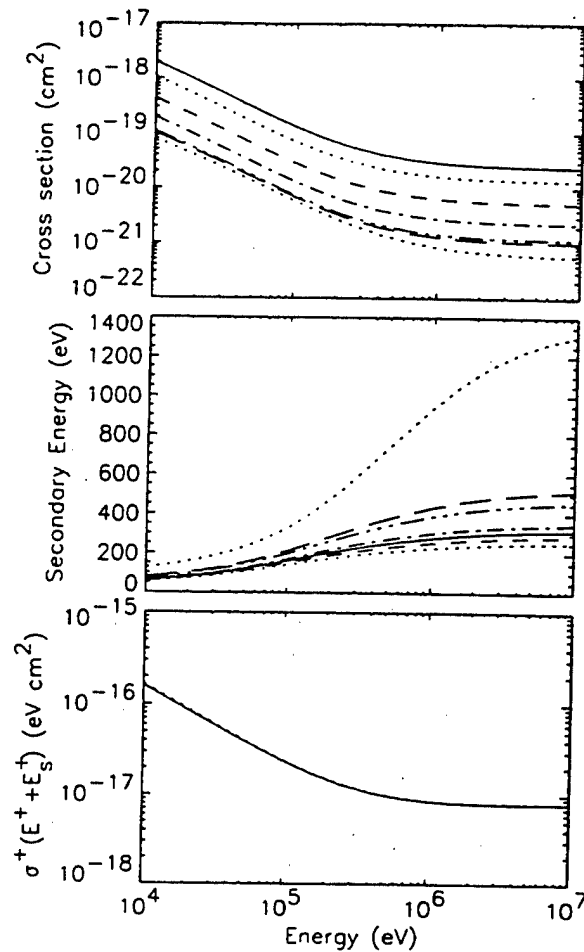
Figure 4.6: Cross sections, average secondary energies, and total energy-loss cross section for molecular oxygen.

4.2 Khazanov4D Model Simulations

The Khazanov4D model was modified to include relativistic effects. Several test cases were conducted to ensure proper simulation, and an example case is shown below. Results using the model are also reported in *Khazanov et al.* [1999]

For the results below, the model was run with one energy step 0.25 MeV wide centered at 5 MeV, injected at 700 km at pitch angles greater than 40° (upward direction only). The injection was assumed to be Gaussian with a width of 0.5 MeV. It was run with a time step of 10^{-4} s for an L=2 field line (ionospheric latitude near 45°, with an equatorial plane crossing at 2 R_E geocentric). The injection lasted one time step, and then the beam was allowed to decay with time. This configuration was chosen because it illustrates the longest lifetime of a relativistic beam injection from the ionosphere. That is, by injecting at 700 km, particles with large pitch angles will mirror, or bounce (due to the inhomogeneous geomagnetic field), in the upper ionosphere, before they experience excessive collisions with atmospheric neutral particles (which we feel will be the largest loss mechanism for these particles). Also, because the simulations do not include the effects of plasma waves (either externally-generated waves, like hiss and whistlers, or self-generated waves due to the unstable nature of the beam

46

$$N_{tot} \propto \int \frac{B_i}{B} ds \int d\mu \int \frac{\phi}{\sqrt{E}} dE \qquad (4.8)$$

The solid line is the same run as shown in the previous plots, while the dotted line shows the results from a run with no scattering or loss mechanisms included (except loss to altitudes below 200 km). It is seen that after the initial loss of particles due to the injection pitch angle range spanning part of the loss cone, the model does not have significant loss of particles. Also seen is the exponential decrease in the number of particles as seen in Figures 4.7 and 4.8. The half-life of the beam particle count is 0.68 s.
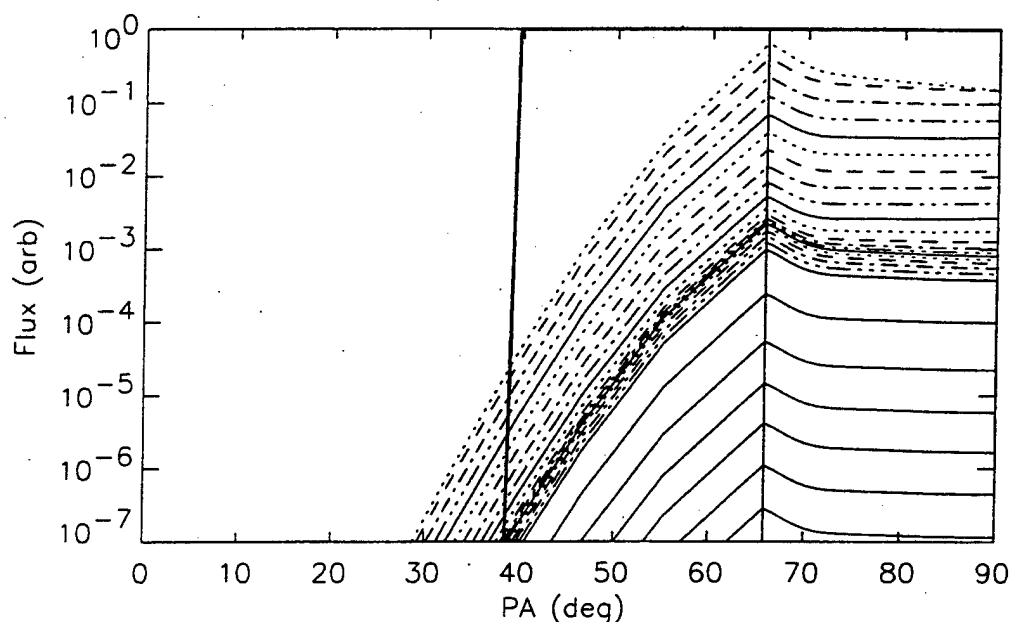

Figure 4.7:   Downward fluxes at the injection location (700 km altitude in the northern ionosphere) as the beam passes by this spatial point. The results are for successive bounces of the beam, with the heavy line being the initial distribution and a solid line every 5th bounce.

Figure 4.8: Particle trajectories and pitch angle definitions in the s-μ and s-μ_0 planes.

Figure 4.9: Downward fluxes at the injection location (700 km altitude in the northern ionosphere) integrated for the entire beam pass over this spatial point. The results are for successive bounces of the beam, with the heavy line being the initial distribution and a solid line every 5th bounce.
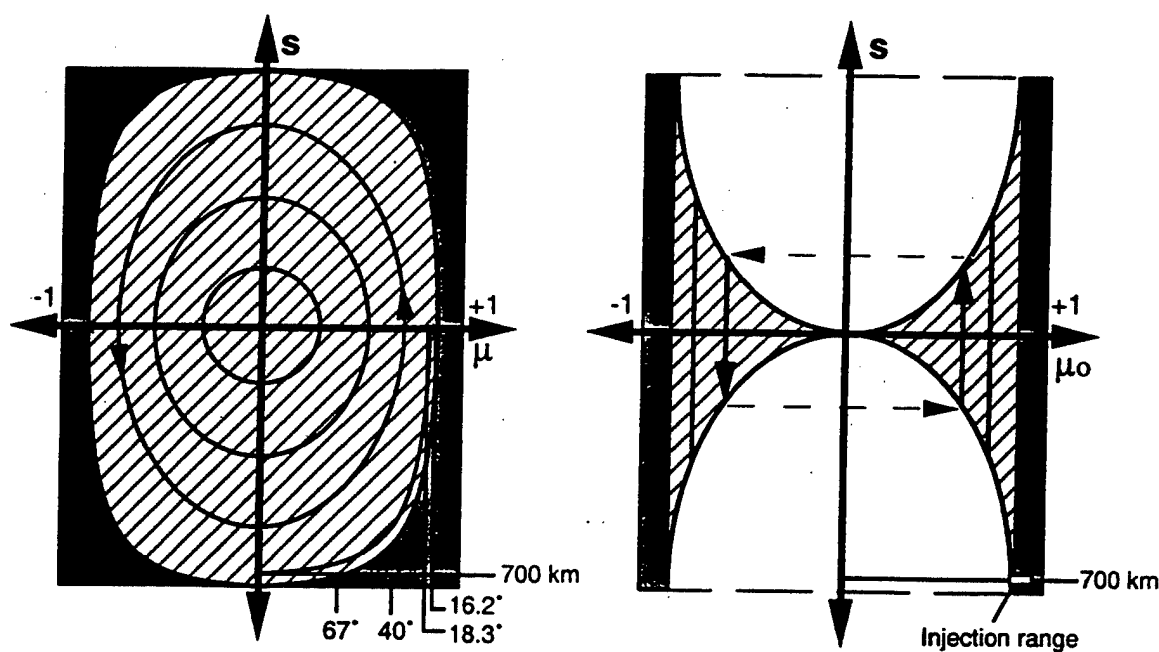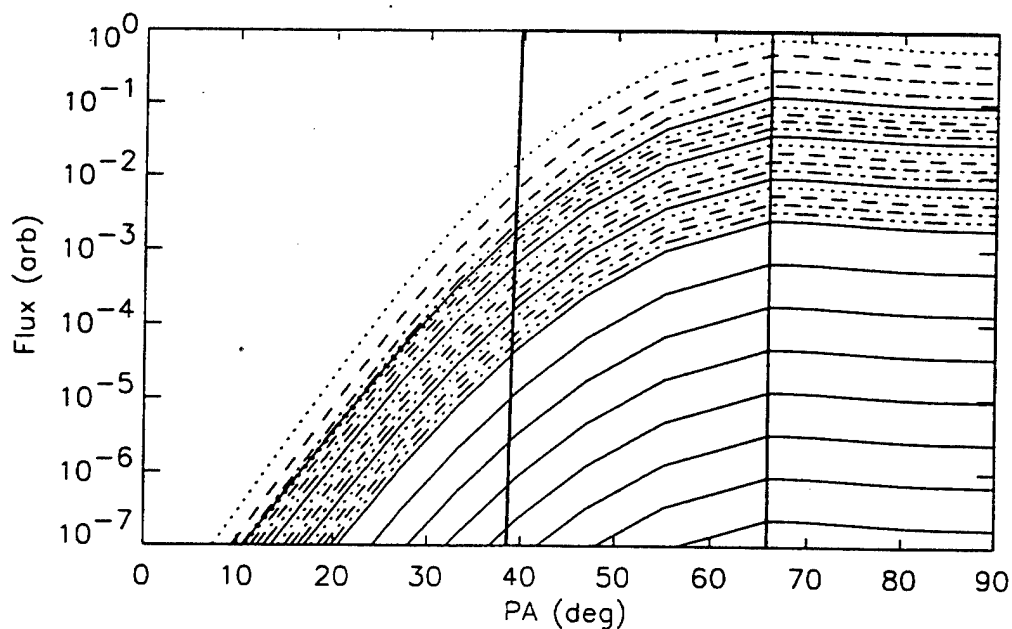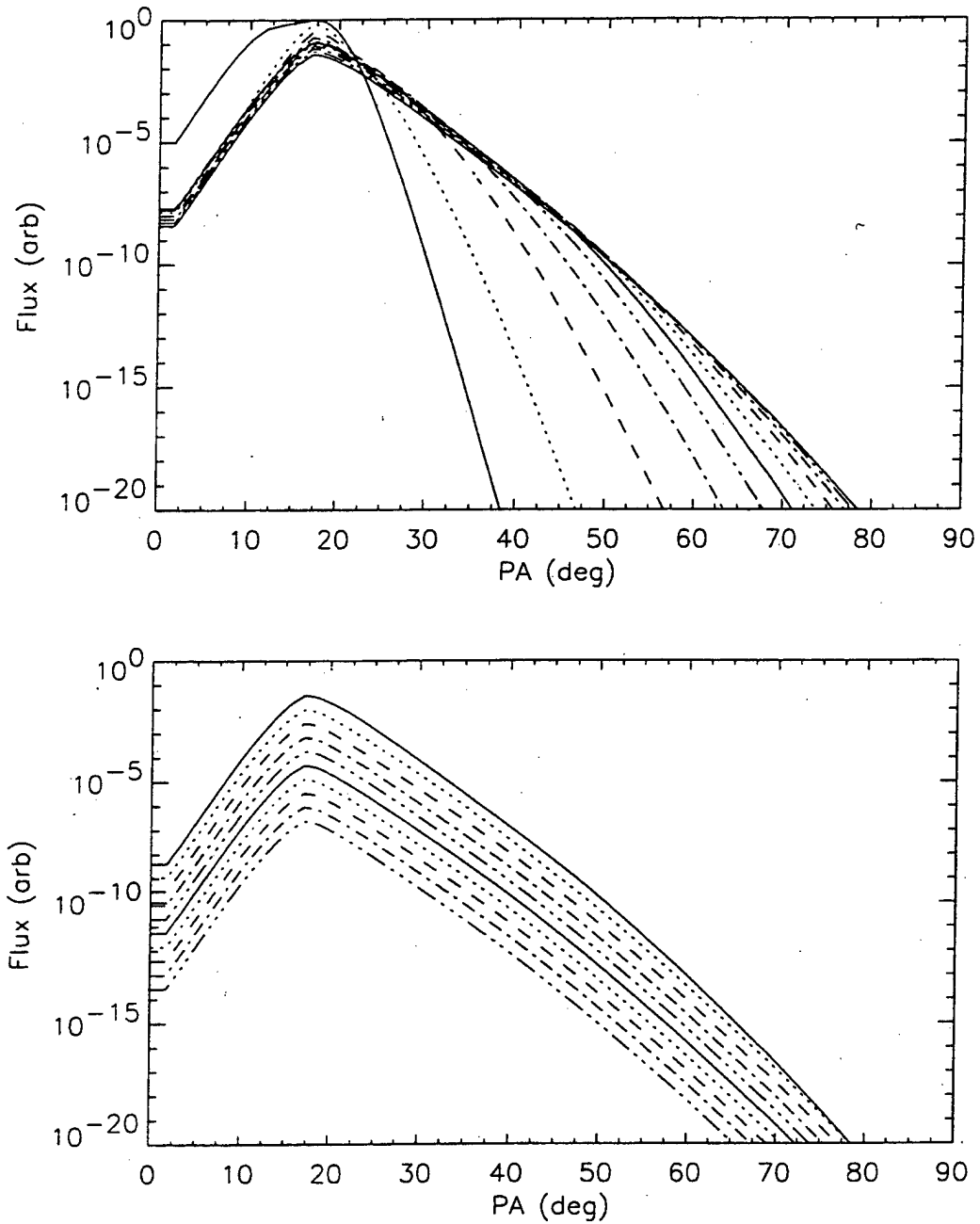
Figure 4.10: Equatorial pitch angle distributions during successive bounces of the injected beam. The upper panel shows results for the first 2 s with a curve every bounce period, and the lower panel shows results for the next 8 seconds, with a curve every 5th bounce. The trapped zone flux is increasing in the upper panel, but is then decreasing in lower panel.
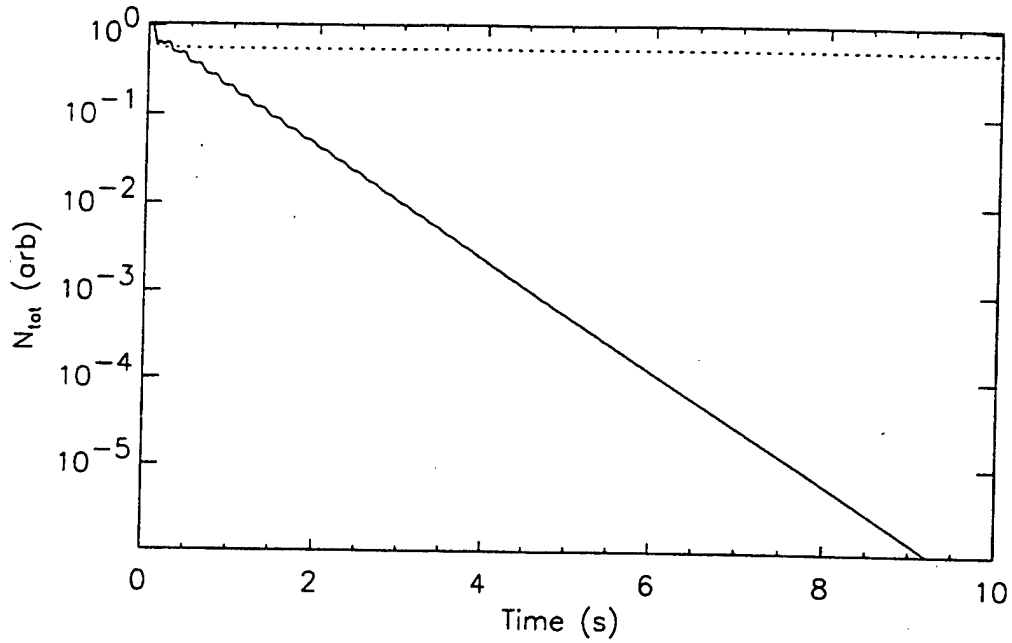
Figure 4.11: Total beam particle evolution for a run with scattering/losses (solid line) and without scattering/losses (dotted line).

4.3 Khazanov5D Injection Configuration

The configuration of the injected relativistic electron beam is the same as that used for the Khazanov4D model, as discussed in *Khazanov et al.* [1999]. It assumes an upward injection from 700 km altitude in the ionosphere, with particle loss to the atmosphere occurring at 200 km. The beam is injected with a Gaussian energy spectra centered on 5 MeV with a 0.5 MeV width, and an intensity that is constant with pitch angle. The energy grid is divided into 9 cells 0.25 MeV wide, the lowest one centered on 4 MeV and the highest one centered on 6 MeV. The equatorial pitch angle grid is chosen so that 5 grid cells fit exactly within trapped part the beam injection region (that is, that part of the beam that mirrors above 200 km), and then the cell size smoothly enlarges toward 0° and 90°. For L=2, 3, and 4, this trapped injection range is 2.33°, 1.13°, and 0.67° wide centered about 18.37°, 9.39°, and 5.95°, respectively. For the initial MLT distribution, a Gaussian centered about local noon with a 0.25 hour spread was assumed. This is not only for numerical stability, avoiding sharp gradients in the variable of greatest advective drift, but also to simulate the initial spread of the injected beam over 1 bounce.

50

4.3.1 Model Parameters

The collisional operators in the kinetic equation require information about the neutral atmosphere and thermal plasma. For these background quantities, the standard models of MSIS-90 and IRI-90 are used at spring equinox of 1991. This represents a solar maximum condition when collisional losses are expected to be greatest. The equatorial plane thermal plasma densities are taken from a quiet time result from the Rasmussen plasmaspheric model, which is the standard dynamic plasmasphere model used in the Khazanov5D model.

Wave-particle interaction diffusion coefficients are calculated using the method of *Albert* [1999]. Four wave types are included in the wave-particle diffusion coefficient calculation: plasmaspheric hiss; lightning-generated whistlers; and two bands of VLF transmitter signals. All are right-hand polarized whistler-mode waves with Gaussian distributions in both frequency and wave propagation angle. The characteristics used for these waves are those given by *Abel and Thorne* [1998].

These background particle and wave characteristics are used to calculate pitch angle scattering and energy loss coefficients. A representative sample of the diffusion coefficients is shown in Figure 4.12 at several spatial locations. The scattering rates for each type of wave as well as that for particle collisions are presented, as well as the initial condition pitch angle range for reference. It is clear that collisional scattering is only effective for pitch angles that reach the atmosphere, with this coefficient rising by two orders of magnitude over its plasmaspheric value. The wave coefficients are dominated everywhere by the interaction with hiss, and drop significantly at lower pitch angles. However, the scattering rate at the inner edge of the injection range is roughly equal for the two processes at $L=2$ and 3, and they are within a factor of 2 at $L=4$. The roughness in the VLF coefficients is due to the narrowness of the frequency bandwidth for these waves.
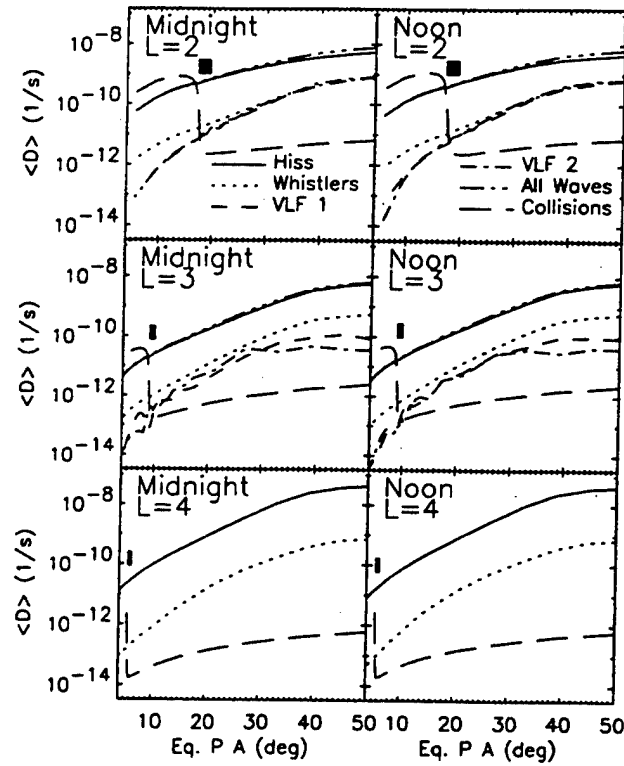
Figure 4.12: Magnitudes of the bounce-averaged pitch angle diffusion coefficients versus equatorial pitch angle at $L=2$, 3, and 4 and at MLT=midnight and noon for 5 MeV electrons interacting with hiss (solid line), lightning whistlers (dotted line), the VLF1 band (dashed line), the VLF2 band (dash-dot line), all waves (dash-dot-dot-dot line), and particles (long dashed line). The small black boxes indicate the pitch angle injection range.

A sample of the collisional energy loss rates is given in Figure 4.13 at several spatial locations and several pitch angles near the injection regions. Again note the dramatic increase (of 2+ orders of magnitude) in loss rate for pitch angles mirroring in the atmosphere. The dashed line is at the center of the initial injection range, yet the loss rate is minor compared to that at the loss cone edge. Figures 4.13 and 4.14 will be discussed in more detail below.
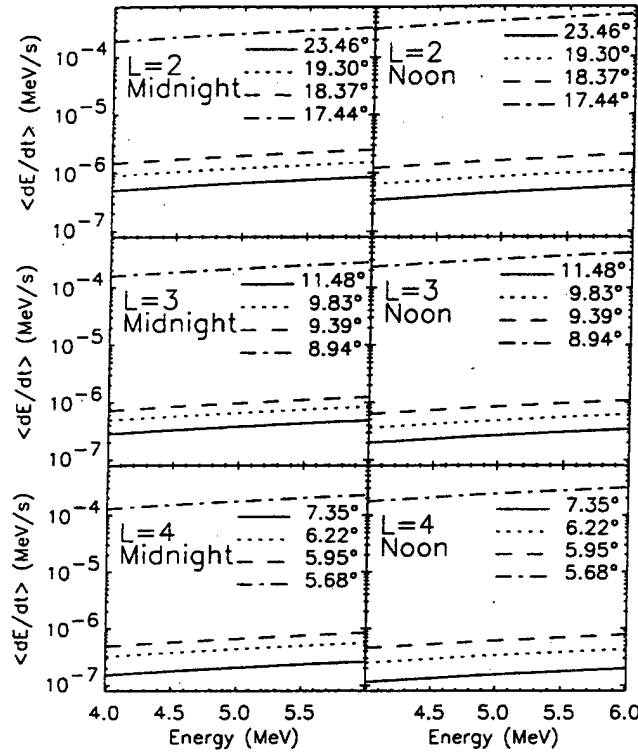
Figure 4.13: Magnitudes of the bounce-averaged energy loss coefficients for several equatorial pitch angles at L=2, 3, and 4 and at MLT=noon and midnight.

4.3.2 Global Representation

In order to examine the global evolution of an injected relativistic electron beam in the inner magnetosphere, simulations were conducted using the above-mentioned initial and background conditions for L=2, 3, and 4 (41.8°, 52.5°, and 58.2° magnetic latitude at 700 km). The gyration-averaged, bounce-averaged, time-dependent, relativistic kinetic equation was solved for the distribution function of the beam electrons as a function of time, azimuth (MLT), energy, and equatorial pitch angle. Because the calculation is linear, the results presented below are given in normalized units and can be scaled to match any beam injection intensity.

Figure 4.14 shows the distribution function versus energy and MLT for the pitch angle cell at the midpoint of the initial condition region for L=2. These results are for simulations with all processes included (drift, collisions, and wave interactions). The contours are spaced every half order of magnitude, and the normalization is scaled to the maximum value at t=0. As the simulation progresses, the beam splits into a series of packets (at all three L values). This is a numerical effect from choosing

only 9 energy grid cells. The dotted line through the packets demarks the drift pattern at each time. With infinitely many energy grid cells, the result at t>0 would look similar to the result at t=0 but tilted along this dotted line and collisionally spread. After two drift periods, the 6 MeV electrons are about to lap the 4 MeV electrons, and a banded structure appears in the energy spectra. While the simulation results still have a beaded-string appearance along the dotted line, the reality (replicated by interpolating between the beads along the dotted line) is a multiply-spiked energy spectra at all local times (banded torus). After a few hours, the overlap is severe. The packets are also spreading due to collisions and scattering. At 6 hours, the packets overlap to such a degree that interpolating them along the dotted lines (as the beam is in reality) forms a non-banded torus around the Earth. As the simulation progresses, the packets eventually disappear (even in spite of the coarse energy grid) and the beam has become (numerically and physically) a smooth torus of relativistic electrons at the L shell of injection.
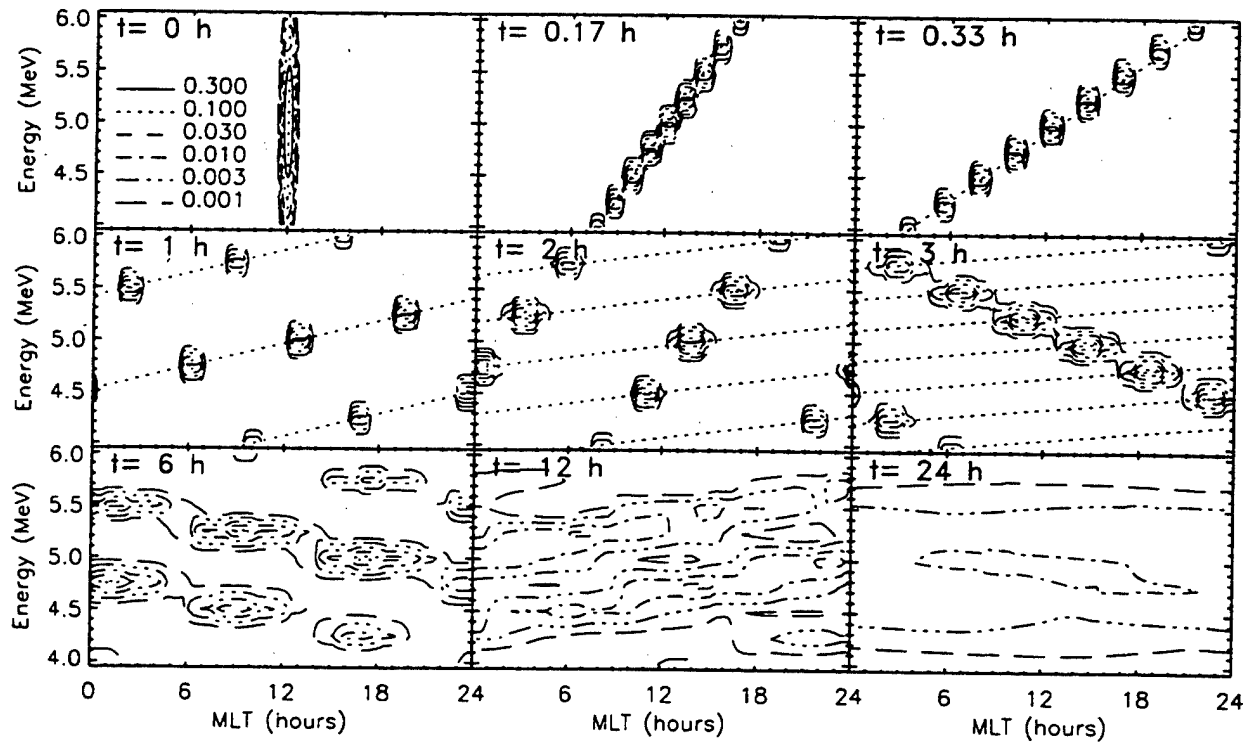
Figure 4.14: The beam distribution versus energy and MLT for 18.4° and $L=2$ at various times.

Figure 4.15 shows the pitch angle versus MLT distributions at 5 MeV for the same simulations as in Figure 4.14. These results are also normalized to the peak value of the initial condition (t=0). The initial condition shows a narrow Gaussian in MLT and uniform distribution across the pitch angle range between the pitch angles that mirror between 200 km in one conjugate hemisphere and 700 km in the

opposite hemisphere. Because the drift differential across the pitch angle injection range is less than for the energy range, the beam does not split into packets, and actually appears as a tilted version of the initial distribution. An interesting feature develops in addition to this tilting effect: a leading population forms right at the edge of the 200 km loss cone. This feature lengthens, broadens, and intensifies with time. This feature is due to collisional energy losses. This term is strongest right near the edge of the loss cone where the electrons mirror deep in the atmosphere and encounter a large number of scattering targets. As the higher energy electrons continue to outpace the 5 MeV electrons shown, they continue to deposit decayed electrons at local times farther and farther ahead of the beam location. The beam, meanwhile, is diffusing in pitch angle (and thus in MLT via the drift differential), eventually becoming a broad band of electrons at all MLT. After one day, this band is more than 100% wider than the initial injection width. Because of the smallness of the pitch angle drift differential, however, significant structure still exists in this band, with an oblique ridge as a distinctive remnant of the original injection configuration.
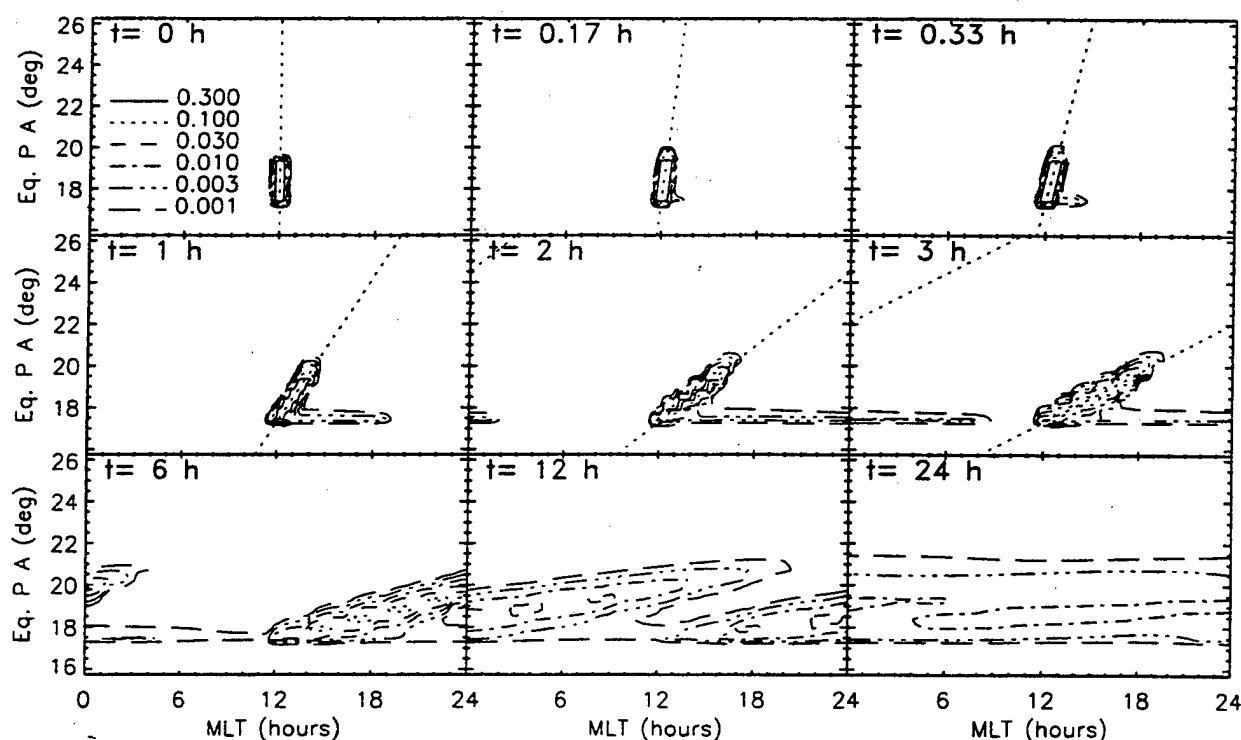

Figure 4.15: The beam distribution versus equatorial pitch angle and MLT for 5 MeV and L=2 at various times.

4.3.3 Total Beam Particle Content

With so much differential spreading over MLT, it is difficult to extract the magnitude of the beam loss as a function of time from plots of the distribution function. A useful quantity to examine, therefore, is the total number of particles in the beam. This quantity is found by integrating the distribution function over all phase space at a given time. Figure 4.16 presents this quantity for various simulations. The upper panel shows results at $L=2$ for azimuthal transport (drift) only, drift plus collisions, drift plus wave interactions, and all processes included. First, the simulation for drift only solidly maintains its original number of particles. This is encouraging, because atmospheric loss was not omitted from this calculation (it is included in all of these simulations), and the scattering and loss operators were also not omitted, simply calculated with coefficients of zero. This means that there was no numerical diffusion from these calculations. This is also seen in plots similar to Figures 4.14 and 4.15 (not plotted, however), which show the simulation maintaining the original functional form of the beam. Secondly, this plot shows that waves are more important at this L shell than collisions with particles for removing electrons from the beam, but collisions are not an insignificant process. Note that it is not a linear addition of the two loss amounts to yield the result when all processes are included, but there is actually less loss in this case. This is because there is only a limited number of particles in the initial beam, and once they are scattered into the loss cone, no matter what process does it, they are gone from the simulation.

The lower panel of Figure 4.16 shows the total particle count for simulations with all processes included at various L. While the beam loses 35% of its particles after 24 hours at $L=2$, it only loses 30% at $L=3$, but loses 60% at $L=4$. The decay rates at t=24 h for the three simulations are 0.99%/h, 0.94%/h, and 1.75%/h, which are all slowly decreasing with time. Compare these late-stage loss rates to the loss rates 1 hour after injection: 2.4%/h, 2.6%/h, and 13.8%/h for the 3 L values, respectively. These results can be explained by reexamining Figures 4.12 and 4.13. The coefficients in those plots can be roughly converted into time scales of particle energy loss or scattering through an E or μ_0 interval. Right at the loss cone edge, it should take about 0.8, 1, and 1.4 hours for an electron to lose 1 MeV of energy for $L=2$, 3, and 4, respectively (note that it takes orders of magnitude longer at pitch angles away from the loss cone edge). The scattering time scale at the loss cone edge is about 3.5, 3.3, and 0.6 hours for $L=2$,

3, and 4, respectively. The dramatic drop for $L=4$ is because the width of the pitch angle injection shrinks with L faster than the diffusion coefficient. These time scales are crude estimations for a single energy and pitch angle, and not global decay rates for all phase space.

The lower panel of Figure 4.16 can now be viewed in terms of the relative magnitudes of these loss rates. The initial loss rate is highly dependent on the scattering rate at the edge of the loss cone, because this is a sharp gradient next to a precipitation zone. The order of the initial loss rates of the L shells match our scattering time scale estimations. The late-stage loss rate is caused by a combination of scattering and decay losses. While $L=3$ has a similar diffusion loss rate to that of $L=2$, the energy loss rate is smaller and thus the beam retains more of its particles. $L=4$ however has a much faster diffusive loss rate that overcomes the slower energy loss rate to result in a larger late-stage loss rate (and reduced beam intensity) at this L value.
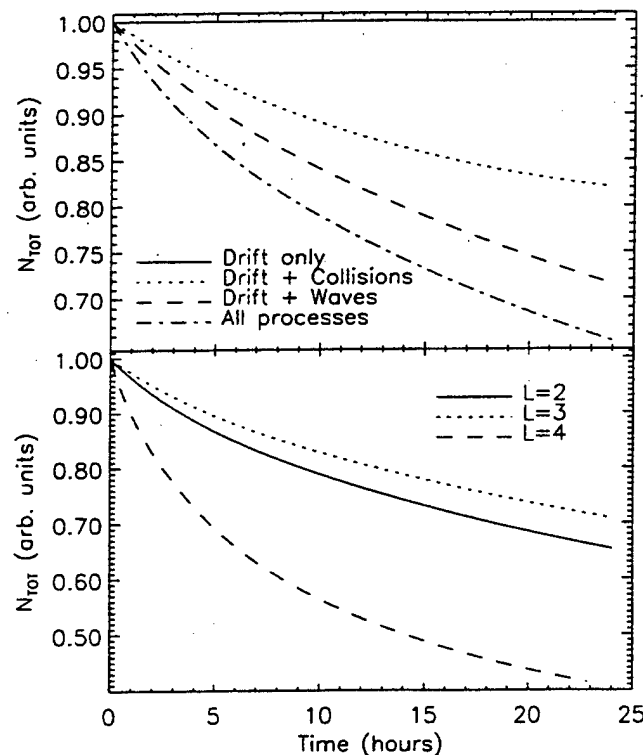

Figure 4.16: Evolution of the normalized total number of particles of the beam at $L=2$ for several simulations with various processes included (upper panel) and at several L values with all processes included (lower panel).

4.4 Khazanov Modeling Summary

In order to examine the global evolution of an artificially injected relativistic electron beam, the bounce-averaged relativistic kinetic equation was solved for the electron distribution function for various scenarios. It was found that the beam quickly spreads in MLT due to differential drift rates. This, combined with energy loss and pitch angle diffusion, eventually transform the beam into a fairly uniform torus around the Earth. It was determined that wave interactions are slightly more important than collisional losses in reducing the $L=2$ beam content. It was also found that the beam total particle loss rate is complicated function of L and initial condition parameters, and for the chosen conditions, a beam at $L=4$ drops much faster than a injected beam at $L=2$ or 3. These loss rates are about 1-2%/h one day after injection, with the beam total particle counts at 65%, 70%, and 40% of the initial count at this time. Other interesting features in the distribution function were examined, such as the leading edge population in the pitch angle-MLT plots, banded structures in the energy spectra, and reasons for the values of the early and late stage decay rates.

A final note of discussion is on the comparison of total loss rates determined in this study with those of our previous study [Khazanov et al., 1999]. There, a time scale of 265 s was stated for an e-folding of the beam intensity. However, because of the very small time step required to resolve the field-aligned structure of the beam, those simulations were only conducted for the first 10 s after injection. As indicated above, the loss rate is initially quite high but then dramatically decreases during the first few hours after injection. In fact, the decay rates for all simulations are still declining after 24 hours. Thus, the Khazanov et al. [1999] value is a good estimate of the initial decay rate of the beam, while this study has examined a different time regime.

Later studies, based on this relativistic model development, have also shown that the beam particles strongly depend on the initial pitch angle distribution and that lifetimes similar to those found for the radiation belts are obtained for nearly equatorial mirroring injections [Khazanov et al., 2000]. It was concluded that the Khazanov et al. [1999] results, which only considered upper ionospheric injections, are consistent with other relativistic electron studies and should be regarded as an examination of the loss

cone edge population, whether naturally occurring or artificially injected into near-Earth space. It is also noted that the model is well adapted to the analyses of the radiation belt fine structure evolution and the dynamics of various regions of velocity space.

5. Summary, Recommendations, and Publications

5.1 Summary of Accomplishments and Results

The following represent key accomplishments and results for this project:

- The RelBAI model was developed to allow detailed accounting of beam energy propagation, generation of secondary particles, and radiation effects such as bremsstrahlung;
- The RelBAI model was used to complete analysis of representative cases associated with propagating a relativistic electron beam from low-Earth orbit down in to the atmosphere;
- Dr. Linda Habash Krause completed her Ph.D. based on the development and application of the RelBAI model;
- The RelBAI model was extended beyond the project work described here to include a relativistic electron auroral model to address the time-dependent chemistry necessary to compute optical emissions as a function of altitude and several potential emissions were identified;
- 3D PIC simulation models were developed for the relativistic beam case;
- The PIC modeling indicates that charging effects will only be an issue at ambient plasma densities less than 10^9 m^{-3} for the proposed beam current and duty cycle;
- Ion focusing of the beam will play a role only for beam currents above 10 A, which is well above the proposed beam current;
- PIC results indicate, that for the currents considered for the linac beam, there will be no significant beam-plasma interaction creating undesirable beam dynamics at least within several 10's of kilometers of the injection point;
- For longer propagation, the PIC results suggest the beam will experience scattering in both energy and pitch angle though it will continue to propagate;
- Khazanov4D and Khazanov5D models were extended to relativistic beam energies;
- The Khazanov models showed that the relativistic electron beam quickly spreads in MLT due to differential drift rates and combined with energy loss and pitch angle diffusion, eventually transform the beam into a fairly uniform torus around the Earth;
- The Khazanov models showed that the beam total particle loss rate is complicated function of L and initial condition parameters;

- The Khazanov models showed that the beam particles strongly depend on the initial pitch angle distribution and that lifetimes similar to those found for the radiation belts are obtained for nearly equatorial mirroring injections.

5.2 Recommendations for Future Work

It is recommended to go forward with the relbeam flight program. As a first step, it is proposed to develop an accelerator flight unit for a sounding rocket mission. During flight, the accelerator should inject beam pulses downwards into the upper atmosphere. Simultaneous coordinated observations from ground should be done of optical emissions and radar echoes from density striations. This scenario provides for the best diagnostics configuration of accelerator performance and beam propagation characteristics.

It is further recommended to carry out the experiment in connection with severe thunderstorms, in order to explore electrical processes in connection with thunderstorm electric charge- and discharging. The phenomenon of sprites is now understood to the point where good predictions can be made of time and location of sprites. Typically, sprites occur from well defined thunderstorm cells over a period of 30 minutes or more, during which time the occurrence rate is about one sprite every 2 minutes. The details of sprite generation is not know, but it is thought that a discharge is initiated at 70 km altitude in connection with a positive cloud-to-ground discharge in the storm below. Possibly, the discharge process can be explored with relativistic beams, where seed ionization and electric potential modification is generated down to 40-50 km altitude. It is possible, a relbeam will initiate a discharge. Such experiment would be unique and quite spectacular, if successful. It would represent an added science value to the basic experiment objectives that are to assess accelerator and beam performance in space.

Launch cites must be assessed for their compatibility with the sprite experiments. It is required, that the beam track at 50 km altitude is across a regions with severe thunderstorm activity. White Sands, New Mexico, and Wallops Island may be candidates.

The theoretical results presented here have shown from various points of view that relativistic beam propagation in the ionosphere and magnetosphere appears feasible. By this we mean that the beam is expected to easily escape a spacecraft, that the beam appears generally stable as it propagates initially, and it is possible for the beam to have very large lifetimes. If the beam pitch angle is low enough to be within the loss-cone, the beam can be deposited in the atmosphere.

The models developed under this project are ready and able to focus in on specific potential applications. They can be used to address practical aspects or issues of conducting actual flight

experiments. Concerns with detection methods on the one hand and impacts to other space assets can both be addressed. This would be the next logical steps in this work.

5.3 Publications and Presentations

The following publications and presentations were generated as a result of the work sponsored by this grant.

PUBLICATIONS

Khazanov, G. V., M. W. Liemohn, E. N. Krivorutsky, J. U. Kozyra, and B. E. Gilchrist, Interhemispheric transport of relativistic electron beams, *Geophys. Res. Lett.*, *26*, 581, 1999.

Neubert, T. and B. E. Gilchrist, 3D electromagnetic PIC simulations of relativistic electron pulse injections from spacecraft, *Adv. Space Res., submitted*, 2000.

Khazanov, G. V., M. W. Liemohn, E. N. Krivorutsky, J. U. Kozyra, J. M. Albert, and B. E. Gilchrist, On the influence of the initial pitch angle distribution on relativistic electron beam dynamics, J. *Geophys. Res., 105*, 16093, 2000.

PRESENTATIONS

Habash Krause, L., Analysis of Active Space Experiments Using Artificial Relativistic Electron Beams

Habash Krause, L., T. Neubert, and B. E. Gilchrist, Passive remote sensing of artificial relativistic electron beams in the middle atmosphere, *Proc. AIAA 1999 Space Technology Conference and Exposition*, Norfolk, VA, *AIAA-99-4352,* 1999.

Habash Krause, L., B. E. Gilchrist, and T. Neubert, Analysis of active space experiments with relativistic electron beams, *Proc. 6th International Spacecraft Charging Technology Conference*, Nov. 1998, Hanscom AFB, MA, *in press*, 2000.

Neubert, T. and B. E. Gilchrist, 3D electromagnetic PIC simulations of relativistic electron pulse injections from spacecraft, *COSPAR., July*, 2000.

5. References

Abel, B., and R. M. Thorne, Electron scattering loss in the Earth's inner magnetosphere 2, Sensitivity to model parameters, *J. Geophys. Res., 103*, 2397, 1998.

Albert, J. M., Analysis of quasilinear diffusion coefficients, *J. Geophys. Res., 104*, 2429, 1999.

Banks, P. M., A. C. Fraser-Smith, B. E. Gilchrist, K. J. Harker, L. R. O. Storey, and P.R. Williamson, New concepts in ionospheric modification, AFGL-TR-88-0133, 1987.

Banks, P. M., B. E. Gilchrist, T. Neubert, N. Meyers, W. J. Raitt, P. R. Williamson, A. C. Fraser-Smith, and S. Sasaki, Charge-2 rocket observations of vehicle charging and charge neutralization, *Adv. Space Res., 10(7)*, 137-142, 1990.

Berger, M. J., and S. M. Seltzer, Tables of energy losses and ranges of electrons and positrons, *NASA Spec. Publ. No. 3012*, 1964.

Buneman, O., T. Neubert, and K. -I. Nishikawa, Solar wind-magnetosphere interaction as simulated by a 3D, EM particle code, *IEEE Trans. Plasma Sci., 20*, 810, 1992.

Habash Krause, L., Augmentation of high energy beam_induced ionospheric modification experiment, AASERT technical report, University of Michigan Project #32043, 31 July 1997.

Habash Krause, L., Augmentation of high_energy beam_induced ionospheric modification experiment, AASERT technical report, University of Michigan Project #32043, 01 September 1997.

Habash Krause, L., Augmentation of high_energy beam_induced ionospheric modification experiment, AASERT technical report, University of Michigan Project #32043, 31 July 1998.

Habash Krause, L., Augmentation of high_energy beam_induced ionospheric modification experiment, AASERT technical report, University of Michigan Project #32043, 01 September 1998.

Habash Krause, L., T. Neubert, and B. E. Gilchrist, Passive remote sensing of artificial relativistic electron beams in the middle atmosphere, *Proc. AIAA 1999 Space Technology Conference and Exposition*, Norfolk, VA, *AIAA-99-4352*, 1999.

Habash Krause, L., B. E. Gilchrist, and T. Neubert, Analysis of active space experiments with relativistic electron beams, *Proc. 6th International Spacecraft Charging Technology Conference*, Nov. 1998, Hanscom AFB, MA, *in press*, 2000.

Humpries, S., Jr., Charged Particle Beams, Wiley-Interscience Publication, John Wiley and Sons, Inc., 1990.

Jackman, C. H., R. H. Garvey, and A. E. S. Green, Electron impact on atmospheric gases, I, Updated cross sections, *J. Geophys. Res., 82*, 5081, 1977.

Jordanova, V. K., J. U. Kozyra, and A. F. Nagy, Effects of heavy ions on the quasi-linear diffusion coefficients from resonant interactions with electromagnetic ion-cyclotron waves, *J. Geophys. Res., 101*, 19.771, 1996.

Jost, R. J., Space borne relativistic electron accelerator system, Phase 1: feasibility study, PL-TR-93-2113, 1993.

Khazanov, G. V., T. Neubert, and G. D. Gefan, A unified theory of ionosphere-plasmasphere transport of suprathermal electrons, *IEEE Trans. Plasma Sci., 22*, 187, 1994.

Khazanov, G. V., T. E. Moore, M. W. Liemohn, V. K. Jordanova, and M.-C. Fok, Global collisional model of high-energy photoelectrons, *Geophys. Res. Lett., 23*, 331, 1996.

Khazanov, G. V., M. W. Liemohn, J. U. Kozyra, and T. E. Moore, Inner magnetospheric superthermal electron transport: Photoelectron and plasma sheet electron sources, *J. Geophys. Res., 103*, 23,485, 1998.

Khazanov, G. V., M. W. Liemohn, E. N. Krivorutsky, J. U. Kozyra, and B. E. Gilchrist, Interhemispheric transport of relativistic electron beams, *Geophys. Res. Lett., 26*, 581, 1999.

Khazanov, G. V., M. W. Liemohn, E. N. Krivorutsky, J. U. Kozyra, J. M. Albert, and B. E. Gilchrist, On the influence of the initial pitch angle distribution on relativistic electron beam dynamics, *J. Geophys. Res., 105*, 16093, 2000.

Lawson, J. D., The Physics of Charged-Particle Beams, Oxford Science Publications, Clarendon Press, oxford, 1988.

Lehtinen, N. G., U. S. Inan, and T. F. Bell, Trapped energetic electron curtains produced by thunderstorm driven relativistic runaway electrons, Geophys. Res. Lett., 27, 1095, 2000.

Lyons, L. R., Pitch angle and energy diffusion coefficients from resonant interactions with ion-cyclotron and whistler waves, *J. Plasma Phys. 12*, 417, 1974.

Myers, N. B., W. J. Raitt, B. E. Gilchrist, P. M. Banks, T. Neubert, P. R. Williamson, and S. Sasaki, A comparison of current-voltage relationships of collectors in the Earth's ionosphere with and without electron beam emission, *Geophys., Res. Lett., 16*, 365-368, 1989.

Neubert, T. and B. E. Gilchrist, 3D electromagnetic PIC simulations of relativistic electron pulse injections from spacecraft, *Adv. Space Res., submitted*, 2000.

Neubert, T., B. Gilchrist, S. Wilderman, L. Habash, and H. J. Wang, Relativistic electron beam propagation in the Earth's atmosphere: Modeling results, *Gephys. Res. Lett., 23*, 1009, 1996.

Neubert, T., and P. M. Banks, Recent results from studies of electron beam phenomena in space plasmas, *Planet. Space Sci., 40*, 153, 1992.

Parker, L. W., and B. L. Murphy, Potential buildup on an electron-emitting ionospheric satellite, *J. Geophys. Res., 72*, 1631, 1967.

Thompson, D.C., C. Bonifazi, B.E. Gilchrist, S.D. Williams, W.J. Raitt, J.-P. Lebreton, and W.J. Burke, "The Current-Voltage Characteristics of a Large Probe in Low Earth Orbit: TSS-1R Results," *Geophys. Res. Lett.*, Vol. 25 , No. 4, p. 415, 1998.